Single-Phase FLLs Based on Linear Kalman Filter, Limit-Cycle Oscillator, and Complex Bandpass Filter: Analysis and Comparison With a Standard FLL in Grid Applications

Saeed Golestan, *Senior Member, IEEE*, Josep M. Guerrero, *Fellow, IEEE*, Juan C. Vasquez, *Senior Member, IEEE*, Abdullah M. Abusorrah, *Senior Member, IEEE*, and Yusuf Al-Turki, *Senior Member, IEEE*

***Abstract*—Frequency-locked loops (FLLs) create a rather large category of closed-loop synchronization techniques, which have received considerable attention in different engineering applications, particularly for synchronization, signal processing, and control purposes. Focusing on single-phase grid applications, designing FLLs is often based on a second-order generalized integrator (SOGI), and the SOGI-FLL is regarded as a standard structure. Using the linear Kalman filter (LKF), complex bandpass filter (CBF), and circular limit-cycle oscillator (CLO) are some alternative approaches. FLLs based on these filters/elements, which are briefly referred to as the LKF-FLL, 1ϕ-CBF-FLL, and CLO-FLL, have not been well analyzed in the literature, and limited knowledge about their real advantages/disadvantages compared to the SOGI-FLL exists. Covering this gap is the objective of this paper.**

***Index Terms*—Circular limit-cycle oscillator (CLO), complex bandpass filter (CBF), frequency-locked loop (FLL), grid applications, linear Kalman filter (LKF), second-order generalized integrator (SOGI), single-phase systems, synchronization.**

I. Introduction

In RECENT years, with rapid development in power electronic technology, signal processing devices, and control techniques, power electronic converters have received extra attention in different applications, particularly for interfacing alternative energy sources such as wind and photovoltaic systems to the grid [1]. To ensure an efficient and smooth operation, all grid-tied power converters require a unit for the synchronization with this grid [2]. Such a unit can be implemented in different ways. A popular approach is using the concept of frequency locked-loop (FLL) [3].

FLLs are nonlinear feedback control structures with two major parts. The first is a filter that extracts its input signal(s) fundamental component (and its quadrature version in single-phase applications). The second is a frequency estimator that adapts the aforementioned filter to frequency changes. In single-phase grid-connected applications, which this paper focuses on, designing FLLs is often based on a second-order generalized integrator (SOGI), which is a double-integrator structure with an infinite gain at the fundamental frequency. Fig. 1 illustrates the continuous-time implementation of the SOGI-FLL which, as mentioned before, is a standard single-phase FLL [3]. The SOGI-FLL includes a SOGI-based bandpass filter (BPF)/low-pass filter (LPF)[1] for extracting the input signal fundamental component and its 90° phase-shifted version and a frequency estimator for estimating the grid frequency and adapting the SOGI center frequency to variations of the grid frequency. The amplitude normalization (which is for decoupling the frequency

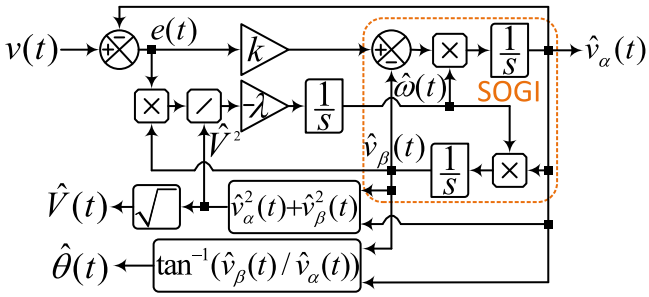

Fig. 1. Continuous-time implementation of the SOGI-FLL. $\hat{v}_\alpha$ is an estimate of the fundamental component of the input signal v, and $\hat{v}_\beta$ is its 90° phase-shifted version. λ is the frequency estimator control parameter, and k is the SOGI gain. $\hat{V}$, $\hat{\omega}$, and $\hat{\theta}$ are estimations of the amplitude, angular frequency, and phase angle of the fundamental component of the input signal v, respectively.

Manuscript received November 15, 2018; revised February 5, 2019; accepted March 10, 2019. Date of publication March 17, 2019; date of current version September 6, 2019. This work was supported by the Deanship of Scientific Research (DSR) at King Abdulaziz University, Jeddah, under Grant D-005-135-1440. Recommended for publication by Associate Editor S. ElMoursi. *(Corresponding author: Saeed Golestan.)*

S. Golestan, J. M. Guerrero, and J. C. Vasquez are with the Department of Energy Technology, Aalborg University, Aalborg DK-9220, Denmark (e-mail:

[1]The transfer function relating $\hat{v}_\alpha$ to v in Fig. 1 is a BPF centered at $\hat{\omega}$, and the transfer function relating $\hat{v}_\beta$ to v is an LPF.

estimator dynamics from grid voltage amplitude variations) and the phase estimator are optional parts which, depending on the application in hand, may be used in the SOGI-FLL structure. In grid applications, where the grid voltage amplitude may undergo large variations (e.g., because of voltage sags or faults), employing the amplitude normalization is highly recommended.

The SOGI-FLL suffers from some shortcomings. The limited disturbance (dc offset, harmonic, and interharmonic) rejection capability is probably the main drawback of this FLL. To deal with this problem, some modifications to enhance the SOGI-FLL filtering capability have been suggested in recent years. For example, to address the dc offset problem, incorporating a dc offset rejection/estimation loop into the SOGI-FLL structure is presented in [4]. To selectively reject harmonic components and, at the same time, to provide estimates of these harmonics, including multiple parallel SOGIs centered at these harmonic frequencies in the SOGI-FLL structure is suggested in [3]. To completely block the dc component and effectively attenuate all harmonics and interharmonics, using one or more adaptive BPFs as a prefiltering stage or an in-loop filter of the SOGI-FLL is suggested and investigated in [5]–[7].

Designing single-phase FLLs, however, is not always based on a SOGI. In fact, they may also be implemented using alternative filters/elements, such as a linear Kalman filter (LKF) [8]–[10], complex bandpass filter (CBF) [11], and circular limit-cycle oscillator (CLO) [12]. A brief review of single-phase LKF-, CLO-, and CBF-based FLLs will be presented in the following sections. Contrary to the SOGI-FLL and its advanced versions, which have been well analyzed in the literature, limited works on the aforementioned FLLs have been conducted. Therefore, their advantages/disadvantages compared to the SOGI-FLL are not very clear. To bridge this gap in knowledge, a thorough analysis of the LKF-FLL, 1ϕ-CBF-FLL,[2] and CLO-FLL is carried out here. The SOGI-FLL is considered as a base for the comparison. The rest of this paper is organized as follows.

In Section II, the focus is on the LKF-FLL and its close variants. After providing a brief review of the LKF-FLL, which is an inherently discrete control system, its continuous-time equivalent is derived. This presentation clearly shows the LKF-FLL structural differences/similarities compared to the SOGI-FLL and facilitates finding the fair condition of comparison between them. Two steady-state versions of the LKF-FLL, which use fixed Kalman gains (instead of adaptive ones in the LKF-FLL), are then introduced, and a detailed comparison between them and the SOGI-FLL under a fair condition is conducted. It has to be emphasized here that introducing and analyzing these steady-state LKF-FLLs (SSLKF-FLLs), regardless of demonstrating their potentiality for applying in grid applications instead of the original LKF-FLL, facilitates achieving the main goal of this part, which is providing a deep insight into the LKF-FLL pros and cons. Finally, the LKF-FLL is analyzed and compared with its steady-state versions and the SOGI-FLL.

Section III deals with the 1ϕ-CBF-FLL. This section is started with a review of this FLL structure. For the sake of simplicity in the analysis, a second-order CBF is first considered in the 1ϕ-CBF-FLL structure, and the small-signal modeling and tuning aspects are discussed. A performance comparison between this 1ϕ-CBF-FLL and the SOGI-FLL is then conducted to gain a deeper insight into its advantages/disadvantages. Finally, some problems of the 1ϕ-CBF-FLL are highlighted, and some solutions are presented.

In Section IV, the paper focuses on the CLO-FLL. The review of its operating principle, its analysis and comparison with the SOGI-FLL, and discussions about its advanced versions are the main parts of this section.

Finally, Section V concludes this paper.

[2] 1ϕ comes here to emphasize that this CBF-FLL is for single-phase applications. Notice that the CBF-FLL is a standard FLL in three-phase applications.

II. LKF-FLL and Its Close Variants

A. Review of LKF-FLL

The Kalman filter is an algorithm for estimating unknown variables (states) of a linear dynamical system from measurements that are noisy and linearly related to the system states. Introducing the Kalman filter dates back to the early 1960s [13], [14]. Since then, the Kalman filter has been developed by different researchers and has been used in different applications. The lifetime and state-of-charge estimation of batteries [15], power system state estimation [16], and designing phase-locked loops [17], [18] are some interesting examples in power and energy applications.

Recently, the LKF application for designing single-phase FLLs has been presented in the literature [8]–[10]. The LKF-FLL uses an LKF for extracting the grid voltage fundamental component and its quadrature version and a frequency estimator similar to that of the SOGI-FLL (see Fig. 1) for detecting the grid frequency and adapting the LKF to frequency changes. Notice that the frequency-adaptive extraction of the grid voltage fundamental component using only the Kalman filter demands an extended Kalman filter, which is a nonlinear and computationally demanding algorithm [8]. The block diagram of the LKF-FLL can be observed in Fig. 2(a). The operating principle of this structure is discussed in more details in what follows.

Developing the LKF in Fig. 2(a) is based on the state-space model as follows [8]–[10]:

$$\boldsymbol{x}(n+1) = \boldsymbol{A}(n)\boldsymbol{x}(n) + \boldsymbol{\varepsilon}(n) \tag{1a}$$

$$y(n) = \boldsymbol{C}(n)\boldsymbol{x}(n) + \gamma(n) \tag{1b}$$

in which the following holds.

1) n indicates the current sample.
2) $\boldsymbol{x}(n) = \left[\, v_\alpha(n)\ v_\beta(n) \,\right]^T$ is the state vector.
3) $\boldsymbol{A}(n)$ is the state transition matrix and is expressed as

$$\boldsymbol{A}(n) = \begin{bmatrix} \cos(T_s\omega(n)) & -\sin(T_s\omega(n)) \\ \sin(T_s\omega(n)) & \cos(T_s\omega(n)) \end{bmatrix} \tag{2}$$

   where T_s is the sampling period (throughout this paper, $T_s = 0.0001$ s is considered, unless otherwise stated) and ω is the grid voltage angular frequency.
4) $y(n)$ is the measurement.
5) $\boldsymbol{C}(n) = \left[\, 1\ 0 \,\right]$ is the measurement matrix.

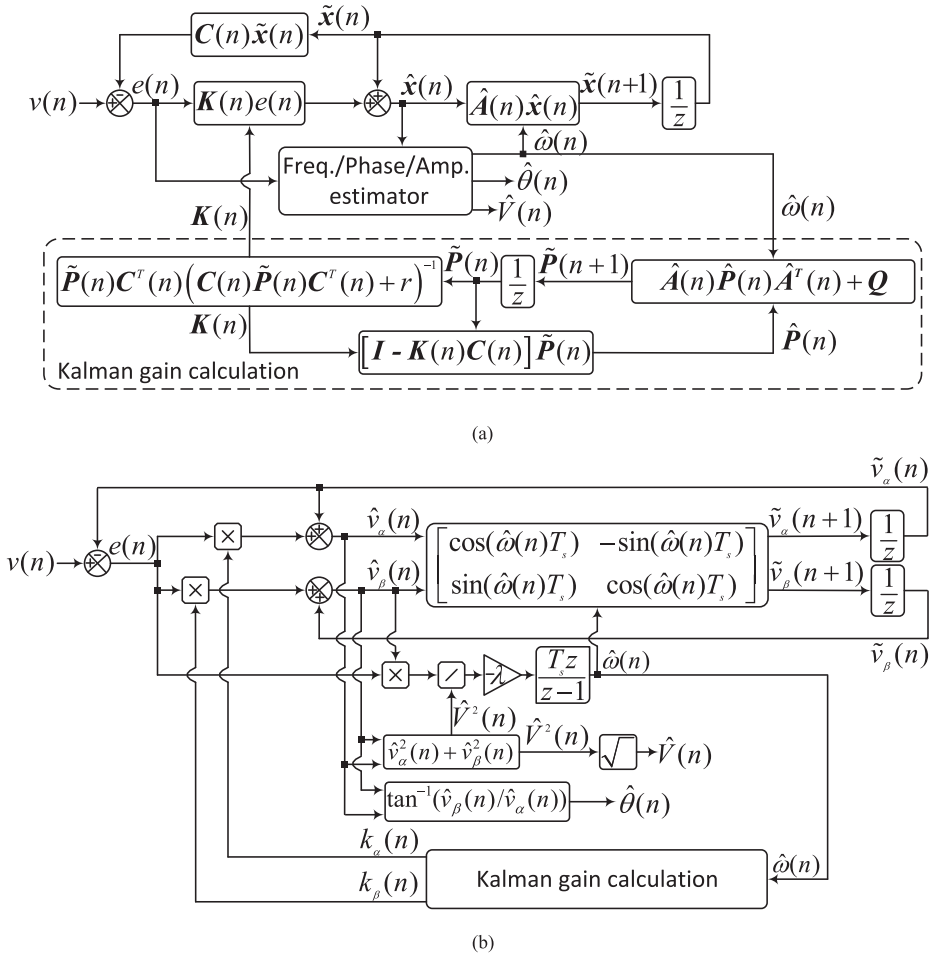

Fig. 2. (a) Block diagram representation of the LKF-FLL. (b) Alternative representation of the LKF-FLL. The bold letters denote a vector or matrix.

6) $\boldsymbol{\varepsilon}(n) \sim N(0, \boldsymbol{Q})$ is the process noise vector, which is assumed to have a zero mean and a covariance matrix equal to $\boldsymbol{Q} = q\boldsymbol{I}$ ($\boldsymbol{I}$ is an identity matrix).
7) $\gamma(n) \sim N(0, r)$ is the measurement noise, which is assumed to be independent from $\boldsymbol{\varepsilon}(n)$ and have a zero mean and a covariance equal to r (r is a scalar because there is only one measured output).

Based on the aforementioned model and assuming that we have *a priori* knowledge of $\boldsymbol{Q}$ and r, the LKF for extracting the grid voltage fundamental component and its 90° phase-shifted version can be implemented by applying the following prediction-correction algorithm [8]–[10]:

Prediction

$$\tilde{\boldsymbol{x}}(n+1) = \hat{\boldsymbol{A}}(n)\hat{\boldsymbol{x}}(n) \tag{3a}$$
$$\tilde{\boldsymbol{P}}(n+1) = \hat{\boldsymbol{A}}(n)\hat{\boldsymbol{P}}(n)\hat{\boldsymbol{A}}^{T}(n) + \boldsymbol{Q}$$

Correction

$$\hat{\boldsymbol{x}}(n) = \tilde{\boldsymbol{x}}(n) + \boldsymbol{K}(n)\left[\boldsymbol{v}(n) - \boldsymbol{C}(n)\tilde{\boldsymbol{x}}(n)\right]$$
$$\boldsymbol{K}(n) = \tilde{\boldsymbol{P}}(n)\boldsymbol{C}^{T}(n)\Big(\boldsymbol{C}(n)\tilde{\boldsymbol{P}}(n)\boldsymbol{C}^{T}(n) + r\Big)^{-1} \tag{3b}$$
$$\hat{\boldsymbol{P}}(n) = \left[\boldsymbol{I} - \boldsymbol{K}(n)\boldsymbol{C}(n)\right]\tilde{\boldsymbol{P}}(n).$$

In (3), $\hat{\boldsymbol{x}}(n)$ and $\tilde{\boldsymbol{x}}(n+1)$ denote an estimate of the state vector and its prediction in the next sample, respectively, and $\hat{\boldsymbol{P}}(n)$ and $\tilde{\boldsymbol{P}}(n+1)$ are their corresponding error covariance matrices. $\boldsymbol{K}(n) = \left[k_\alpha(n)\ k_\beta(n)\right]^T$ is the Kalman gain vector, which is recursively calculated/updated in each sampling period. Additionally, $\hat{\boldsymbol{A}}(n)$ is an estimate of the state transition matrix [see (2) and (4)] as

$$\hat{\boldsymbol{A}}(n) = \begin{bmatrix} \cos(T_s\hat{\omega}(n)) & -\sin(T_s\hat{\omega}(n)) \\ \sin(T_s\hat{\omega}(n)) & \cos(T_s\hat{\omega}(n)) \end{bmatrix}. \tag{4}$$

Notice that $\hat{\omega}$, which is an estimation of the grid angular frequency, is provided by a frequency estimator in Fig. 2(a). This frequency detector, as mentioned before, is the same as that of the SOGI-FLL (see Fig. 1). Considering the aforementioned details, an alternative representation of the LKF-FLL can be obtained, as shown in Fig. 2(b).

A natural question to ask here is whether the LKF-FLL is a better option than the SOGI-FLL. An attempt to answer this question has been made before. In [10], a performance comparison between the LKF-FLL and SOGI-FLL using some numerical tests has been conducted, and it has been concluded that the LKF-FLL has a faster dynamic response and a lower harmonic filtering capability than the SOGI-FLL. These conclusions, nevertheless, do not provide any reliable information about the true relationship between the LKF-FLL and SOGI-FLL mainly because they are based on selecting arbitrary control parameters

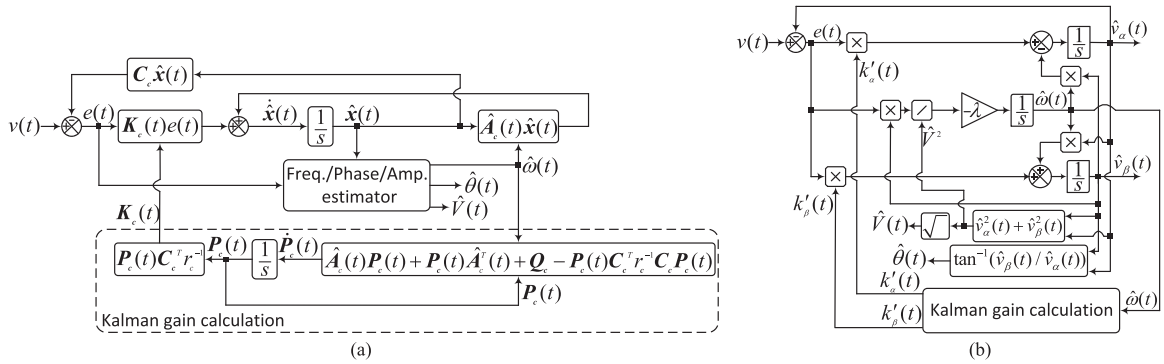

Fig. 3. (a) Continuous-time representation of the LKF-FLL. (b) Its alternative representation.

for these FLLs. To gain a deeper insight into the LKF-FLL characteristics, a more thorough investigation of this FLL will be conducted in what follows.

B. Continuous-Time Equivalent of LKF-FLL

The LKF-FLL analysis is slightly difficult because it is a discrete-time control algorithm. To deal with this problem, the LKF-FLL continuous-time equivalent is presented in this section.

The first step toward the aforementioned objective is obtaining the continuous-time equivalent of (1). For this purpose, the state vector $\boldsymbol{x}(n)$ is subtracted from both sides of (1a), and the result is multiplied by $1/T_s$. These operations yield

$$\begin{aligned} &\frac{\boldsymbol{x}(n+1)-\boldsymbol{x}(n)}{T_s} = \frac{1}{T_s}\left(\boldsymbol{A}(n)-I\right)\boldsymbol{x}(n)+\frac{1}{T_s}\boldsymbol{\varepsilon}(n) \\ &y(n) = \boldsymbol{C}(n)\boldsymbol{x}(n)+\gamma(n) \end{aligned} \tag{5}$$

where

$$\begin{aligned} \frac{1}{T_s}\left(\boldsymbol{A}(n)-\boldsymbol{I}\right) &= \frac{1}{T_s}\begin{bmatrix} \cos(T_s\omega(n))-1 & -\sin(T_s\omega(n)) \\ \sin(T_s\omega(n)) & \cos(T_s\omega(n))-1 \end{bmatrix} \\ &\approx \begin{bmatrix} 0 & -\omega(n) \\ \omega(n) & 0 \end{bmatrix}. \end{aligned} \tag{6}$$

In the continuous-time domain, (5) is corresponding to

$$\begin{aligned} \dot{\boldsymbol{x}}(t) &= \boldsymbol{A_c}(t)\boldsymbol{x}(t)+\boldsymbol{\varepsilon_c}(t) \\ y(t) &= \boldsymbol{C_c}(t)\boldsymbol{x}(t)+\gamma_c(t) \end{aligned} \tag{7}$$

where

$$\begin{aligned} \boldsymbol{x}(t) &= \left[\, v_\alpha(t)\ v_\beta(t)\,\right]^T \\ \boldsymbol{A_c}(t) &= \begin{bmatrix} 0 & -\omega(t) \\ \omega(t) & 0 \end{bmatrix} \\ \boldsymbol{C_c}(t) &= \begin{bmatrix} 1\ 0 \end{bmatrix} \\ \boldsymbol{\varepsilon_c}(t) &\sim N(0, \underbrace{\boldsymbol{Q}/T_s}_{\boldsymbol{Q_c}}) \\ \gamma_c(t) &\sim N(0, \underbrace{T_s r}_{r_c}). \end{aligned} \tag{8}$$

Using (3), (7), and (8), the continuous-time error covariance, Kalman gain vector, and estimate update equations can be expressed as [19]

$$\textbf{Error covariance update}$$

$$\begin{aligned} \dot{\boldsymbol{P}}_{\boldsymbol{c}}(t) &= \hat{\boldsymbol{A}}_{\boldsymbol{c}}(t)\boldsymbol{P_c}(t)+\boldsymbol{P_c}(t)\hat{\boldsymbol{A}}_{\boldsymbol{c}}{}^T(t)+\boldsymbol{Q_c} \\ &\quad -\boldsymbol{P_c}(t)\boldsymbol{C_c^T}\boldsymbol{r_c^{-1}}\boldsymbol{C_c}\boldsymbol{P_c}(t) \end{aligned} \tag{9a}$$

$$\textbf{Kalman gain}$$

$$\boldsymbol{K_c}(t) = \boldsymbol{P_c}(t)\boldsymbol{C_c}{}^T r_c^{-1} \tag{9b}$$

$$\textbf{Estimate update}$$

$$\dot{\hat{\boldsymbol{x}}}(t) = \hat{\boldsymbol{A}}_c(t)\hat{\boldsymbol{x}}(t)+\boldsymbol{K_c}(t)\left[v(t)-\boldsymbol{C_c}\hat{\boldsymbol{x}}(t)\right]. \tag{9c}$$

Using (9), the continuous-time representation of the LKF-FLL can be obtained, as shown in Fig. 3(a), or equivalently as Fig. 3(b). This continuous-time representation considerably simplifies the LKF-FLL analysis.

Notice that the discrete-time Kalman gain vector in Fig. 2, i.e., $\boldsymbol{K}(n)=\left[\,k_\alpha(n)\ k_\beta(n)\,\right]^T$, is not a sampled version of the continuous-time one in Fig. 3, i.e., $\boldsymbol{K_c}(t)=\left[\,k'_\alpha(t)\ k'_\beta(t)\,\right]^T$. It is indeed a sampled version of $T_s\boldsymbol{K_c}(t)$ when T_s tends to zero [19].

C. Analysis of Steady-State LKF-FLL (SSLKF-FLL)

Implementing the LKF-FLL, as shown in Fig. 3, involves updating its Kalman gains in each sampling period based on the Kalman filter theory. It is the main structural difference of the LKF-FLL compared to the SOGI-FLL (see Fig. 1). It suggests that to simplify the LKF-FLL analysis and gain a deeper insight into its advantages/disadvantages compared to the SOGI-FLL, it may be a good idea to analyze its steady-state version first. Fig. 4 illustrates the steady-state LKF-FLL (SSLKF-FLL), which uses fixed Kalman gains. An analysis of this structure is conducted in what follows. Two different cases are considered.

1) Simple Case: As it will be discussed in Section II-C2, the steady-state solution of the continuous-time Riccati equation (9a) gives an optimal relationship between the continuous-time Kalman gains k'_α and k'_β in the SSLKF-FLL. In this section, however, this optimal relationship is neglected, and a simple case ($k'_\beta=0$) is considered. In this case, Fig. 4 can be represented as Fig. 5, which is referred to as the simplified SSLKF-FLL. The simplified SSLKF-FLL has a very similar structure to that of the SOGI-FLL (see Fig. 1). Therefore, they are expected to have

TABLE I
CONTROL PARAMETERS OF THE SOGI-FLL, LKF-FLL AND ITS STEADY-STATE VERSIONS, 1ϕ-CBF-FLL, AND CLO-FLL

	Parameters
SOGI-FLL [20]	$k=\sqrt{2},\ \lambda=49\,384$
Simplified SSLKF-FLL	$k'_\alpha=k\omega_n=444.3,\ k'_\beta=0,\ \lambda=49\,384$
SSLKF-FLL	$k'_\alpha=k\omega_n=444.3,\ k'_\beta=2\omega_n-\sqrt{4\omega_n^2+(k'_\alpha)^2}=-141.2\ ,\ \lambda=49\,384$
LKF-FLL	$q/r=T_s^2q_c/r_c=T_s^2\left[(k'_\beta)^2-2\omega_nk'_\beta\right]=0.00109\ ,\ \lambda=49\,384$
1ϕ-CBF-FLL	$\omega_{p1}=151.7,\ \omega_{p2}=62.8,\ \tau=0.0384$
CLO-FLL	$k'=k=\sqrt{2},\ \lambda'=\lambda/\omega_n=157.2$

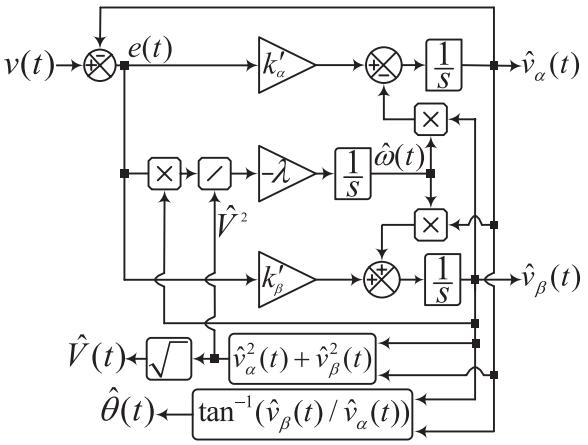

Fig. 4. Block diagram of the SSLKF-FLL. The continuous-time Kalman gains k'_α and k'_β are constant in this structure.

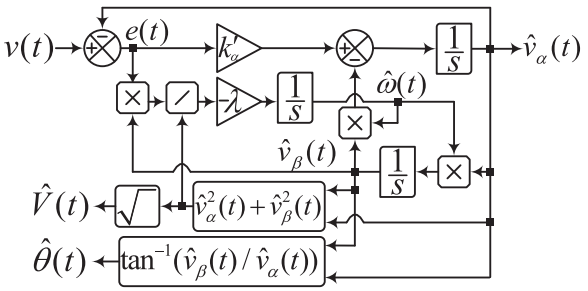

Fig. 5. Simplified SSLKF-FLL.

almost the same performance. This prediction is tested in what follows.

In [7], a small-signal model for the SOGI-FLL is presented. This model can be observed in Fig. 6(a), in which Δ denotes a small perturbation, and $\omega_n=2\pi50$ rad/s is the nominal value of the grid angular frequency. Similarly, a small-signal model for the simplified SSLKF-FLL can be obtained, as illustrated in Fig. 6(b). These models are the same if $k'_\alpha=k\omega_n$. It implies that the simplified SSLKF-FLL and SOGI-FLL are mathematically equivalent systems under the condition mentioned above. Notice that a hidden assumption behind developing the models shown in Fig. 6 (and consequently behind the equivalence of the simplified SSLKF-FLL and SOGI-FLL) is that the frequency of the single-phase input signal is always close to its nominal value. In the grid-connected applications, which is the focus of this paper, this assumption is valid.

To verify the equivalence of the simplified SSLKF-FLL and SOGI-FLL, extensive numerical tests are conducted in the MATLAB/Simulink environment, and their results are presented here. In obtaining these results, the sampling frequency is fixed at 10 kHz. Table I summarizes the selected control parameters. The following tests are considered for the comparison.

1) *Test 1:* The grid voltage undergoes a $+30^\circ$ phase jump.
2) *Test 2:* The grid voltage is subjected to a -3-Hz frequency jump.
3) *Test 3:* The grid voltage experiences a 0.25 p.u. voltage sag.
4) *Test 4:* The grid voltage is contaminated with a dc component of magnitude 0.05 p.u.
5) *Test 5:* The grid voltage is distorted with some low-order harmonics (see Fig. 7 for the grid voltage spectrum).
6) *Test 6:* The grid voltage is polluted with a sub-harmonic component of frequency 1 Hz and magnitude 0.1 p.u.

The solid black and dashed light lines in Fig. 8 illustrate the results of the SOGI-FLL and simplified SSLKF-FLL in response to the tests mentioned above, respectively. The details of these results are summarized in Table II. It can be observed that the simplified SSLKF-FLL and SOGI-FLL have almost identical results. It confirms that they are equivalent systems. Therefore, it can be concluded that the simplified SSLKF-FLL has the same advantages/disadvantages as those of the SOGI-FLL. The performance characteristics of the SOGI-FLL have been already well explained in the literature [7]. Therefore, they are not repeated to save space.

2) Optimal Case: In this section, an optimal relationship between the continuous-time Kalman gains k'_α and k'_β in the SSLKF-FLL is first established. A performance comparison between the SSLKF-FLL and the SOGI-FLL is then conducted.

As pointed out before, the steady-state solution of the continuous-time Riccati equation (9a), which is corresponding to $\dot{\boldsymbol{P}}_{\boldsymbol{c}}(t)=0$, gives an optimal relation between the continuous-time Kalman gains k'_α and k'_β [18], [19]. To this end, the continuous-time error covariance $\boldsymbol{P}_{\boldsymbol{c}}$ is first defined as

$$\boldsymbol{P}_{\boldsymbol{c}}=\begin{bmatrix}p_1 & p_2\\ p_3 & p_4\end{bmatrix} \tag{10}$$

in which $p_2=p_3$ because (9a) is a symmetric equation. Considering this definition, the following equations can be obtained

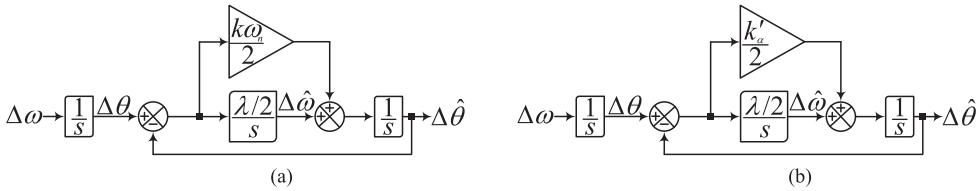

Fig. 6. (a) Small-signal model of the SOGI-FLL [7]. (b) Small-signal model of the simplified SSLKF-FLL.

TABLE II
DETAILS OF SIMULATION RESULTS

	SOGI-FLL	Simplified SSLKF-FLL	SSLKF-FLL	LKF-FLL	1ϕ-CBF-FLL*	LCO-FLL
Test 1						
Phase settling time	25.9 ms (1.3 cycles)	25.6 ms (1.28 cycles)	32.7 ms (1.63 cycles)	32.3 ms (1.62 cycles)	98 ms (4.9 cycles)	32.6 ms (1.63 cycles)
Phase overshoot	13.9° (46.3%)	13.8° (46%)	8° (26.7%)	8.23° (27.4%)	11.19° (37.3%)	10.2° (34%)
Peak frequency deviation	8.15 Hz	8.54 Hz	6.59 Hz	6.65 Hz	1.87 Hz	5.73 Hz
Peak amplitude deviation	0.25 p.u.	0.25 p.u.	0.17 p.u.	0.17 p.u.	0.07 p.u.	0.25 p.u.
Test 2						
Frequency settling time	36.3 ms (1.81 cycles)	34.7 ms (1.73 cycles)	38.2 ms (1.91 cycles)	38.4 ms (1.92 cycles)	77 ms (3.85 cycles)	36.5 ms (1.82 cycles)
Frequency overshoot	0.22 Hz (7.3%)	0.16 Hz (5.3%)	0.12 Hz (4%)	0.14 Hz (4.7%)	0.16 Hz (5.3%)	0.27 Hz (9%)
Peak phase deviation	3.4°	3.3°	3.9°	3.9°	16.17°	3.37°
Peak amplitude deviation	0.03 p.u.	0.03 p.u.	0.02 p.u.	0.02 p.u.	0.04 p.u.	0.03 p.u.
Test 3						
Amplitude settling time	15.6 ms (0.78 cycles)	16.6 ms (0.83 cycles)	20.6 ms (1.03 cycles)	20.6 ms (1.03 cycles)	55 ms (2.75 cycles)	12.9 ms (0.64 cycles)
Amplitude overshoot	0.005 p.u. (2%)	0.007 p.u. (2.8%)	0.005 p.u. (2%)	0.004 p.u. (1.6%)	0.023 p.u. (9.2%)	0.002 p.u. (0.8%)
Peak frequency deviation	0.98 Hz	0.99 Hz	1.53 Hz	1.55 Hz	0.18 Hz	0.79 Hz
Peak phase deviation	3.9°	3.88°	6.03°	6°	2.74°	3.77°
Test 4						
Peak-to-peak frequency error	3.57 Hz	3.68 Hz	2.25 Hz	2.27 Hz	0.25 Hz	3.42 Hz
Peak-to-peak phase error	12.5°	12.9°	7.7°	7.6°	3.5°	12.45°
Peak-to-peak amplitude error	0.18 p.u.	0.19 p.u.	0.12 p.u.	0.12 p.u.	0.06 p.u.	0.18 p.u.
Test 5						
Peak-to-peak frequency error	1.27 Hz	1.3 Hz	1.34 Hz	1.34 Hz	0.19 Hz	1.25 Hz
Peak-to-peak phase error	4.1°	4.2°	3.9°	3.8°	2.62°	4.1°
Peak-to-peak amplitude error	0.05 p.u.	0.05 p.u.	0.06 p.u.	0.06 p.u.	0.05 p.u.	0.05 p.u.
Test 6						
Peak-to-peak frequency error	7.15 Hz	7.43 Hz	4.5 Hz	4.5 Hz	0.31 Hz	6.2 Hz
Peak-to-peak phase error	25°	26°	15.5°	15.3°	4.3°	24.6°
Peak-to-peak amplitude error	0.37 p.u.	0.38 p.u.	0.24 p.u.	0.23 p.u.	0.07 p.u.	0.36 p.u.

*In determining the 1ϕ-CBF-FLL settling time in Test 1, 2, and 3, the double-frequency oscillations in its transient response are neglected and its average dynamic behavior is considered.

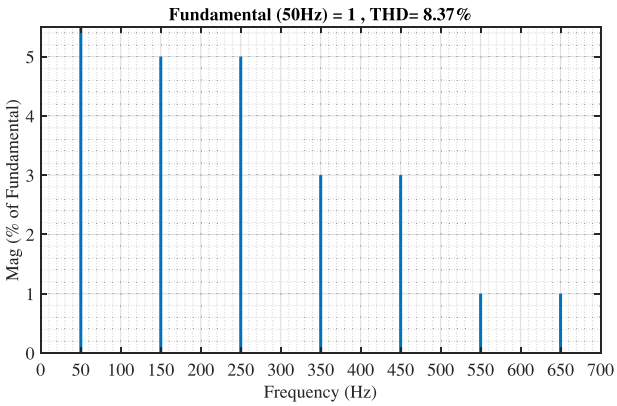

Fig. 7. Grid voltage spectrum in Test 5.

by solving $\dot{\boldsymbol{P}}_{\boldsymbol{c}}(t) = 0$:

$$\begin{aligned} &\frac{1}{r_c}p_1^2 + 2\hat{\omega}p_2 - q_c = 0 \\ &\hat{\omega}p_1 - \frac{1}{r_c}p_1p_2 - \hat{\omega}p_4 = 0 \\ &\frac{1}{r_c}p_2^2 - 2\hat{\omega}p_2 - q_c = 0. \end{aligned} \tag{11}$$

Considering the same definition, i.e., (10), the continuous-time Kalman gain vector (9b) may also be expressed as

$$\boldsymbol{K_c} = \begin{bmatrix} k'_\alpha \\ k'_\beta \end{bmatrix} = \begin{bmatrix} p_1/r_c \\ p_2/r_c \end{bmatrix}. \tag{12}$$

Based on (11) and (12), we have

$$k'_\alpha = \sqrt{q_c/r_c - 2\hat{\omega}^2 + 2\hat{\omega}\sqrt{\hat{\omega}^2 + q_c/r_c}} \tag{13a}$$

$$k'_\beta = \hat{\omega} - \sqrt{\hat{\omega}^2 + q_c/r_c}. \tag{13b}$$

Using (13a) and (13b), the optimal relation between the Kalman gains of the SSLKF-FLL can be obtained as

$$k'_\beta = 2\hat{\omega} - \sqrt{4\hat{\omega}^2 + (k'_\alpha)^2}. \tag{14}$$

Notice that, thanks to this optimal relation, selecting an appropriate value for k'_α automatically determines k'_β. Notice also that in all equations (11), (13), and (14), $\hat{\omega}$ (which is an estimate of the grid voltage angular frequency) is assumed to be a constant.

According to Fig. 4 and by assuming that $\hat{\omega}$ is a constant, the transfer functions relating the output signals $\hat{v}_\alpha(t)$ and $\hat{v}_\beta(t)$ to

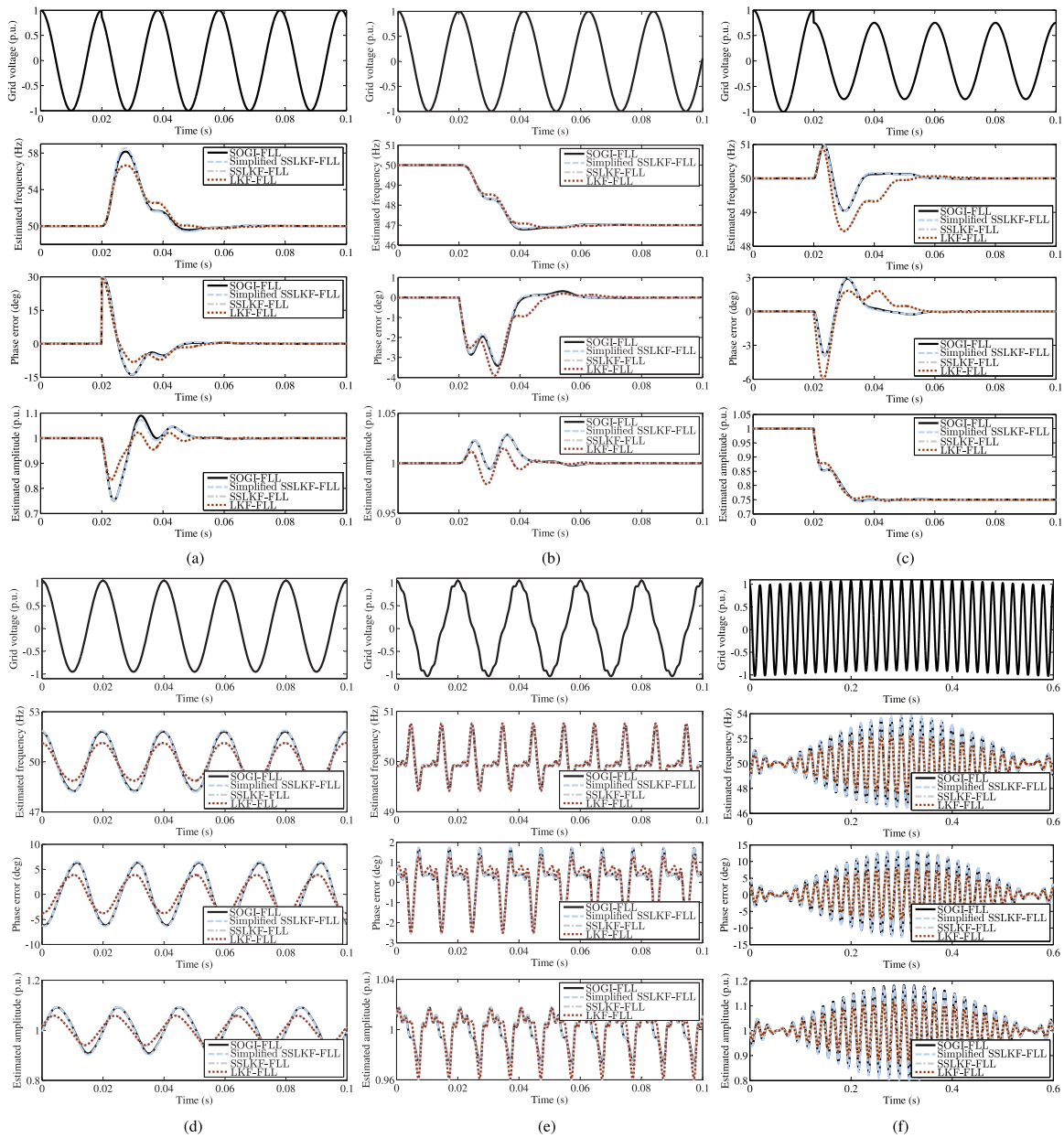

Fig. 8. Performance comparison among the SOGI-FLL, simplified SSLKF-FLL, SSLKF-FLL, and LKF-FLL. (a) Test 1. (b) Test 2. (c) Test 3. (d) Test 4. (e) Test 5. (f) Test 6.

the input signal $v(t)$ in the SSLKF-FLL can be obtained as

$$\hat{v}_\alpha(s) = \frac{k'_\alpha s - k'_\beta \hat{\omega}}{s^2 + k'_\alpha s + \hat{\omega}(\hat{\omega} - k'_\beta)} v_\alpha(s) = \underbrace{\frac{k'_\alpha s - k'_\beta \hat{\omega}}{\left(s + \boldsymbol{k'_\alpha/2}\right)^2 + \hat{\omega}(\hat{\omega} - k'_\beta) - (k'_\alpha/2)^2}}_{G_\alpha(s)} v(s) \quad (15)$$

$$\hat{v}_\beta(s) = \frac{k'_\beta s + k'_\alpha \hat{\omega}}{s^2 + k'_\alpha s + \hat{\omega}(\hat{\omega} - k'_\beta)} v_\alpha(s) = \underbrace{\frac{k'_\beta s + k'_\alpha \hat{\omega}}{\left(s + \boldsymbol{k'_\alpha/2}\right)^2 + \hat{\omega}(\hat{\omega} - k'_\beta) - (k'_\alpha/2)^2}}_{G_\beta(s)} v(s). \quad (16)$$

Both these transfer functions, as highlighted in (15) and (16), have a convergence time constant equal to $2/k'_\alpha$ in response to a step sinusoidal input [18]. For the case of the SOGI-FLL, as highlighted in the following, this time constant is equal to $2/(k\hat{\omega})$:

$$\hat{v}_\alpha(s) = \frac{k\hat{\omega}s}{s^2 + k\hat{\omega}s + \hat{\omega}^2} v(s) = \underbrace{\frac{k\hat{\omega}s}{\left(s + \boldsymbol{k\hat{\omega}/2}\right)^2 + \hat{\omega}^2(1 - k^2/4)}}_{G'_\alpha(s)} v(s) \quad (17)$$

$$\hat{v}_\beta(s) = \frac{k\hat{\omega}^2}{s^2 + k\hat{\omega}s + \hat{\omega}^2} v(s) = \underbrace{\frac{k\hat{\omega}^2}{\left(s + \boldsymbol{k\hat{\omega}/2}\right)^2 + \hat{\omega}^2(1 - k^2/4)}}_{G'_\beta(s)} v(s). \quad (18)$$

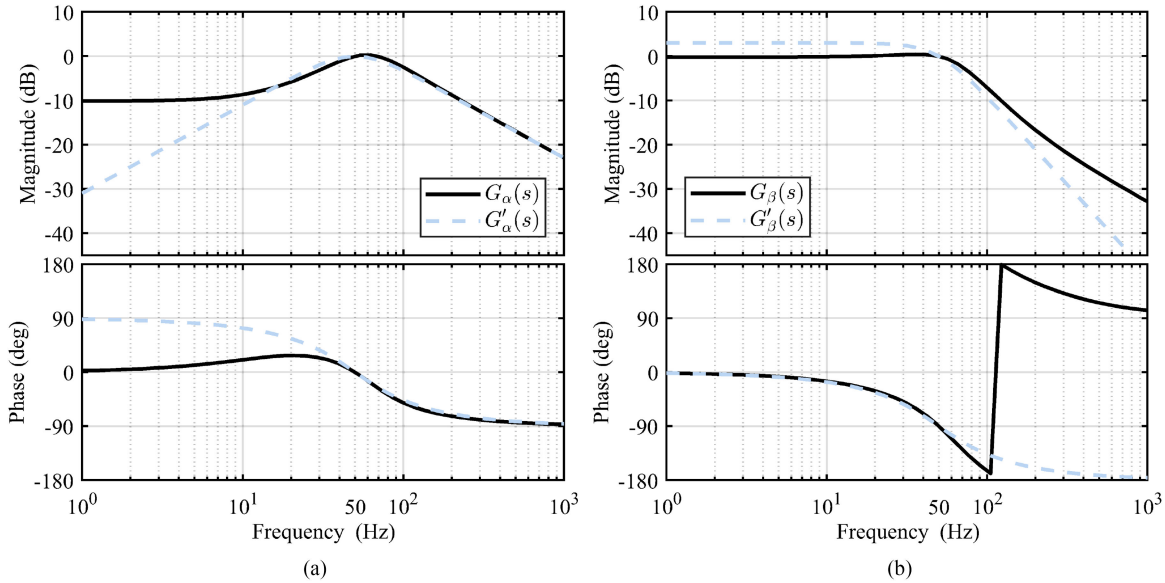

Fig. 9. Bode plots of the characteristic transfer functions of the SSLKF-FLL (solid lines) and SOGI-FLL (dashed lines). (a) Bode plots of (15) and (17) [$G_\alpha(s)$ and $G'_\alpha(s)$]. (b) Bode plots of (16) and (18) [$G_\beta(s)$ and $G'_\beta(s)$].

Therefore, it can be concluded that a fair condition of comparison between the SSLKF-FLL and SOGI-FLL requires $k'_\alpha = k\hat{\omega}$. Based on this condition, (14), and the selected parameters for the SOGI-FLL, the SSLKF-FLL control parameters are determined, as summarized in Table I. Notice that $\hat{\omega} = \omega_n = 2\pi 50$ rad/s is considered in the calculation of the control parameters.

After determining the SSLKF-FLL parameters, a performance comparison with the SOGI-FLL can be conducted to highlight its advantages/disadvantages. To this end, the same condition and tests as those described in Section II-C1 are considered here. The dash–dot lines in Fig. 8 illustrate the results of the SSLKF-FLL in response to these tests (see Table II for more details). According to these results, the following observations are made.

1) The SSLKF-FLL offers a rather higher dc offset and sub-harmonic rejection capability compared to the SOGI-FLL [see Fig. 8(d) and (f), and Table II]. This feature is attributable to the second control gain (the β-axis gain) of the SSLKF-FLL, which results in a lower dc component and sub-harmonic in its β-axis output compared to that of the SOGI-FLL. This fact is clear from Bode plots shown in Fig. 9(b). Notice that the α-axis output of the SSLKF-FLL, contrary to that of the SOGI-FLL, is not free from any dc component and contains a higher level of low-frequency sub-harmonics [see Bode plots shown in Fig. 9(a)]. The aforementioned reduction in the dc/sub-harmonic component of its β-axis output outweighs this drawback.
2) The SOGI-FLL offers a little better performance in attenuating the grid voltage harmonics compared to the SSLKF-FLL [see Fig. 8(e)]. The reason is that, as shown in Fig. 9(b), the transfer function (18) provides a higher attenuation at harmonic frequencies compared to (16).
3) Roughly speaking, the SSLKF-FLL has a slightly slower and more damped dynamic response[3] compared to the SOGI-FLL. This fact is particularly noticeable in the phase jump test results shown in Fig. 8(a).

In summary, the SSLKF-FLL represents a rather higher dc offset/sub-harmonic rejection capability, a little lower harmonic filtering ability, and a slightly slower and more damped dynamic behavior compared to the SOGI-FLL in estimating the grid voltage parameters. These performance differences, however, are not that large to consider one of them much better than the other one. Therefore, this paper concludes that the SSLKF-FLL and SOGI-FLL are systems of roughly comparable qualities.

D. Analysis of LKF-FLL

After investigating the steady-state versions of the LKF-FLL and discussing their performance characteristics compared to the SOGI-FLL, we focus on the LKF-FLL analysis in this section.

The Kalman gain vector of the LKF-FLL, as shown in Fig. 2(a), depends on three factors: 1) the process noise covariance $\boldsymbol{Q} = q\boldsymbol{I}$, 2) the measurement noise covariance r, and 3) the estimated frequency $\hat{\omega}$. Among these factors, the only variable is the third one, i.e., $\hat{\omega}$. This parameter, however, has a limited variation range in the steady state because, in grid applications, which is the focus of this paper, the grid frequency is always close to its nominal value.[4] It implies that the Kalman gains of the LKF-FLL are also always close to their corresponding steady-state values at the nominal frequency. This fact can be observed in Fig. 10. Therefore, it can be concluded that the

[3]The voltage sag test results [see Fig. 8(c)] are not completely consistent with this statement as the estimated quantities by the SSLKF-FLL in this test suffer from a larger transient compared to those of the SOGI-FLL.

[4]According to EN50160 standard, the grid frequency is only allowed to vary in the range of 47–52 Hz [21].

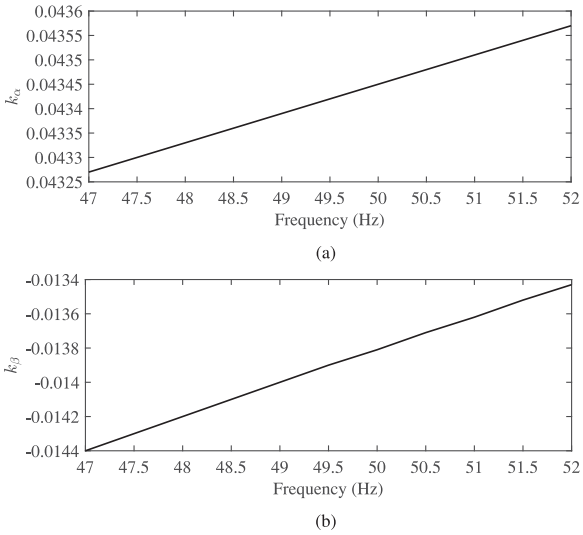

Fig. 10. Variations of the LKF-FLL Kalman gains as a function of the grid frequency. (a) α-axis Kalman gain. (b) β-axis Kalman gain. The grid frequency variation range, according to the EN50160 standard [21], is considered to be 47–52 Hz. $q/r = 0.00109$.

TABLE III
COMPUTATIONAL BURDEN

	States	$\times$	$\div$	$+/-$	ITF[1]	SQRT[2]
SOGI-FLL	3	7	2	3	1	1
Simplified SSLKF-FLL	3	7	2	3	1	1
SSLKF-FLL	3	8	2	4	1	1
LKF-FLL[3]	7	21	2	14	1	1
1ϕ-CBF-FLL[4]	5	14	2	11	1	1
CLO-FLL	3	9	1	5	1	1

[1] ITF: Inverse Trigonometric Function.
[2] SQRT: Square Root.
[3] For the sake of consistency, the computational burden of the LKF-FLL continuous-time equivalent (see Fig. 3) is presented here.
[4] A second-order CBF in the 1ϕ-CBF-FLL structure is used.

LKF-FLL and its steady-state version, i.e., the SSLKF-FLL, should have practically the same performance in the grid-connected applications.

To support the prediction mentioned above, the performance of the LKF-FLL in response to the same tests as those described in Section II-C1 is investigated and compared with that of the SSLKF-FLL. Notice that, according to (8), a fair comparison between the LKF-FLL and SSLKF-FLL requires $q/r = T_s^2 q_c/r_c$. Notice also that the ratio q_c/r_c can be calculated using (13b). The control parameters of the LKF-FLL and SSLKF-FLL can be found in Table I.

The dotted lines in Fig. 8 illustrate the obtained results for the LKF-FLL (see Table II for details). As predicted, these results are practically the same as those of the SSLKF-FLL. Based on this fact, the following conclusions can be made.

1) The SSLKF-FLL is a better option than the LKF-FLL in the grid-connected applications because it uses fixed Kalman gains and, therefore, demands a lower computational effort. Notice that the procedure of calculating the Kalman gain vector in the LKF-FLL imposes a high computational burden. Table III, which summarizes the number of states and mathematical operations required for the implementation of the FLL systems under study, clearly demonstrates this fact.
2) In grid-connected applications, the LKF-FLL has the same performance advantages/disadvantages as those of the SSLKF-FLL compared to the SOGI-FLL (see Section II-C2 for a description of these pros and cons). Considering this fact and its much higher computational burden (see Table III), it can be concluded that it is not an attractive option compared to the SOGI-FLL.

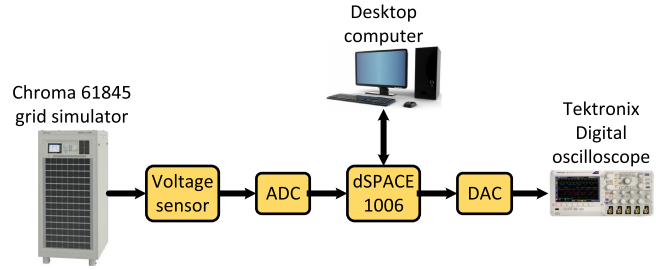

Fig. 11. Experimental setup.

E. Experimental Results

To support the numerical results and the conclusions made based on them, some experimental results are presented in this section. In obtaining these results, as shown in Fig. 11, a Chroma grid simulator is employed for generating the single-phase grid voltage signal. After measuring by a voltage sensor, this signal is fed to the dSPACE 1006 platform through an analog-to-digital converter and is used as the input of the FLL systems under study. The FLLs are processed by the dSPACE, and the estimated quantities by them are sent out using a digital-to-analog converter and displayed on a Tektronix digital oscilloscope. The sampling frequency is 10 kHz, and the grid voltage nominal amplitude and frequency are 100 V and 50 Hz, respectively.

To save space, only one experimental test is performed, in which the grid voltage contains 5 V (0.05 p.u.) dc component. Fig. 12 illustrates the obtained experimental results. It can be observed that the SOGI-FLL and simplified SSLKF-FLL (SSLKF-FLL and LKF-FLL) have practically identical results. It can also be observed that the SSLKF-FLL and LKF-FLL provide a higher dc rejection capability compared to the SOGI-FLL and simplified SSLKF-FLL. These observations are consistent with the numerical results [see Fig. 8(d)].

III. 1ϕ-CBF-FLL

A. Review of 1ϕ-CBF-FLL

Complex filters are characterized by having an asymmetrical frequency response around zero Hertz, which enables them to discriminate positive- and negative-sequence components of imbalanced signals from each other. This feature has made the complex filters very popular in different three-phase signal processing and control applications, particularly in designing controllers and synchronization techniques for three-phase power converters [22]–[24].

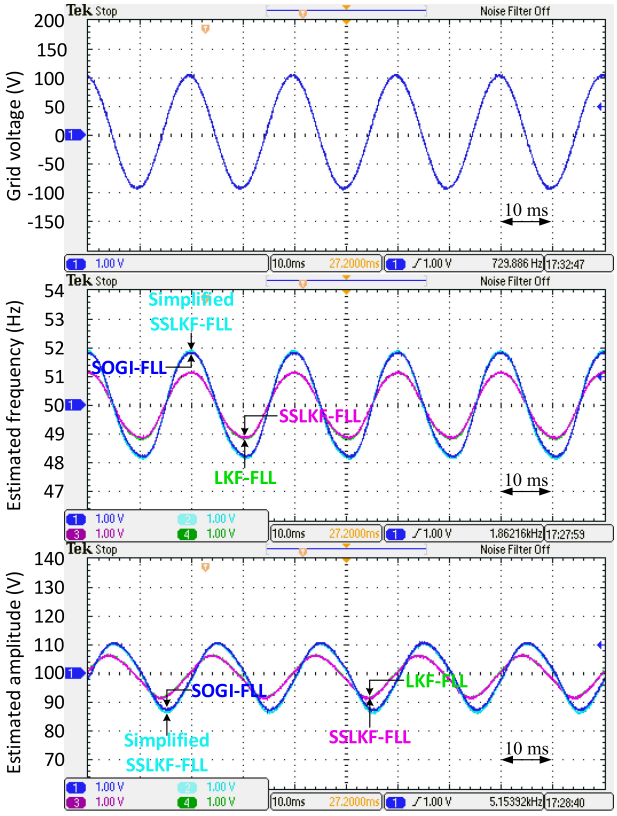

Fig. 12. Experimental performance comparison of the SOGI-FLL, simplified SSLKF-FLL, SSLKF-FLL, and LKF-FLL in the presence of 5 V (0.05 p.u.) dc component in the grid voltage.

In [11], the application of CBFs for designing a single-phase FLL is suggested. The block diagram representation of this idea, which is referred to as the 1ϕ-CBF-FLL, can be observed in Fig. 13(a). The basic idea in designing the 1ϕ-CBF-FLL is that the signal-phase signal $v(t) = V\cos(\theta)$ in its input can be viewed as an imbalanced signal in the $\alpha\beta$ frame as follows:

$$\begin{aligned} 2v(t) &= \overbrace{V\cos(\theta)}^{\text{Pos. seq.}} + \overbrace{V\cos(-\theta)}^{\text{Neg. seq.}} = v_\alpha(t) \\ 0 &= V\sin(\theta) + V\sin(-\theta) = v_\beta(t). \end{aligned} \tag{19}$$

A CBF is then used to get rid of the negative-sequence component and extract the positive one. Notice that this positive-sequence component provides in-phase and quadrature-phase versions of the single-phase input, which are used for calculating the phase, frequency, and amplitude. The estimated frequency is finally passed through a first-order LPF and fed back for adapting the CBF to grid frequency changes.

B. Analysis of 1ϕ-CBF-FLL

The CBF in the 1ϕ-CBF-FLL structure can be of any order and can be implemented in different ways. In this paper, for the sake of simplicity in the analysis, a second-order one as shown in Fig. 13(b) is considered. The basic building block of this CBF, as highlighted in Fig. 13(b), is a reduced-order generalized

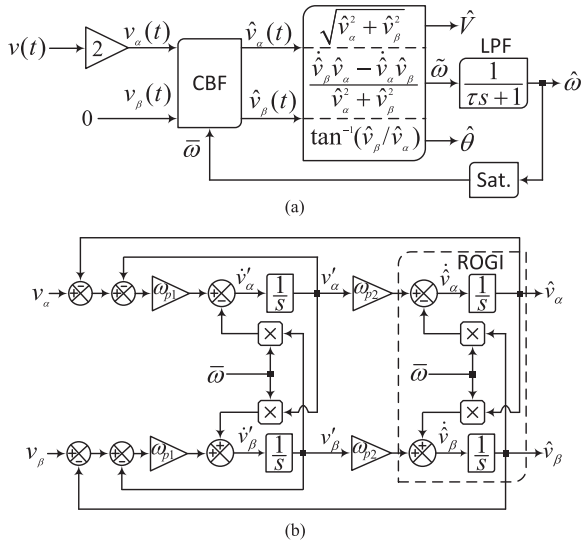

Fig. 13. (a) General block diagram representation of the 1ϕ-CBF-FLL [11] in the continuous-time domain. (b) Continuous-time implementation of a second-order CBF. Sat. denotes a saturation. τ is the time constant of the LPF, and ω_{p1} and ω_{p2} are the control parameters of the second-order CBF.

integrator (ROGI), which is expressed in the Laplace domain as $G_{\text{ROGI}}(s) = \frac{1}{s-j\bar{\omega}}$ [25].[5]

1) Modeling: To the best of authors' knowledge, no model for the 1ϕ-CBF-FLL has yet been presented, which makes its tuning rather difficult. To simplify the tuning procedure of this FLL, its small-signal modeling is presented here.

For deriving a small-signal model for the 1ϕ-CBF-FLL, we have to neglect the negative-sequence component in its input [see (19)]. In this case, the $\alpha\beta$-axis input and output signals of the 1ϕ-CBF-FLL can be expressed as

$$\begin{aligned} v_\alpha(t) &= V\cos(\theta) \\ v_\beta(t) &= V\sin(\theta) \end{aligned} \tag{20}$$

$$\begin{aligned} \hat{v}_\alpha(t) &= \hat{V}\cos(\hat{\theta}) \\ \hat{v}_\beta(t) &= \hat{V}\sin(\hat{\theta}). \end{aligned} \tag{21}$$

We also have to neglect the saturation in Fig. 13(a). In this case, $\bar{\omega} = \hat{\omega}$.

From Fig. 13, we have

$$\dot{\hat{\theta}} = \frac{d}{dt}\left[\tan^{-1}\left(\frac{\hat{v}_\beta}{\hat{v}_\alpha}\right)\right] = \frac{\dot{\hat{v}}_\beta\hat{v}_\alpha - \dot{\hat{v}}_\alpha\hat{v}_\beta}{\hat{v}_\alpha^2 + \hat{v}_\beta^2} = \tilde{\omega} \tag{22}$$

$$\begin{aligned} \dot{\hat{v}}_\alpha &= \omega_{p2}v'_\alpha - \bar{\omega}\hat{v}_\beta \\ \dot{\hat{v}}_\beta &= \omega_{p2}v'_\beta + \bar{\omega}\hat{v}_\alpha. \end{aligned} \tag{23}$$

Substituting (23) into (22) gives

$$\begin{aligned} \dot{\hat{\theta}} = \tilde{\omega} &= \frac{\omega_{p_2}\left[v'_\beta\hat{v}_\alpha - v'_\alpha\hat{v}_\beta\right] + \bar{\omega}\left[\hat{v}_\alpha^2 + \hat{v}_\beta^2\right]}{\hat{v}_\alpha^2 + \hat{v}_\beta^2} \\ &= \underbrace{\frac{\omega_{p_2}}{\hat{V}^2}\left[v'_\beta\hat{v}_\alpha - v'_\alpha\hat{v}_\beta\right]}_{\vartheta} + \bar{\omega}. \end{aligned} \tag{24}$$

[5]In this transfer function representation, the assumption is that the ROGI center frequency $\bar{\omega}$ is a constant.

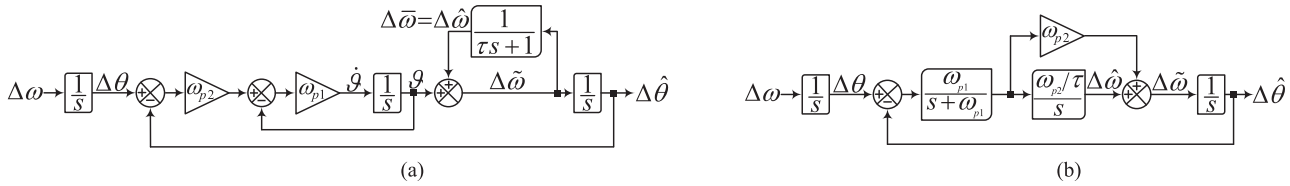

Fig. 14. (a) Small-signal model of the 1ϕ-CBF-FLL. (b) Its alternative representation.

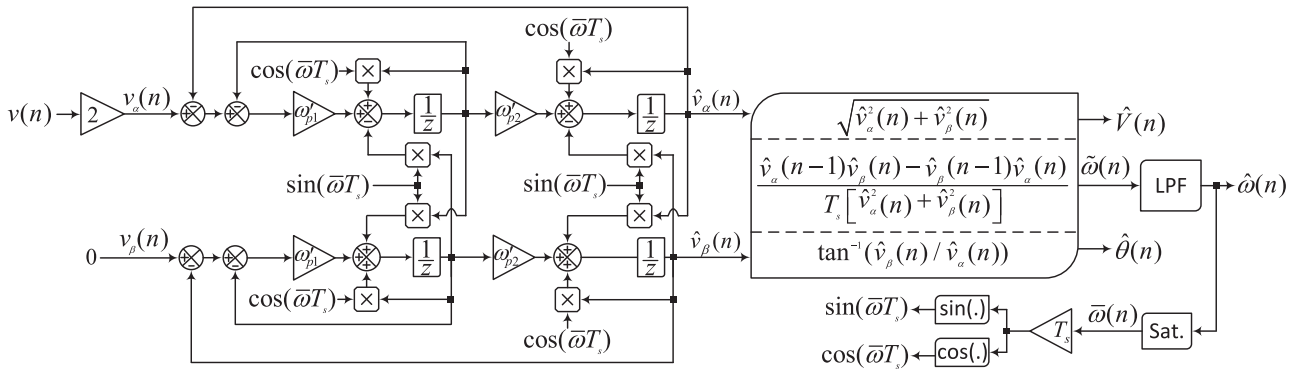

Fig. 15. Digital implementation of the 1ϕ-CBF-FLL. The FLL system, as mentioned before, uses a second-order CBF. $\omega'_{p1} = T_s\omega_{p1}$ and $\omega'_{p2} = T_s\omega_{p2}$.

With neglecting dynamics of $\hat{V}$, differentiating ϑ in (24) with respect to time yields

$$\dot{\vartheta} \approx \frac{\omega_{p_2}}{\hat{V}^2}\left[\dot{v}'_\beta\hat{v}_\alpha + v'_\beta\dot{\hat{v}}_\alpha - \dot{v}'_\alpha\hat{v}_\beta - v'_\alpha\dot{\hat{v}}_\beta\right] \tag{25}$$

where

$$\begin{aligned}\dot{v}'_\alpha &= \omega_{p1}(v_\alpha - \hat{v}_\alpha - v'_\alpha) - \bar{\omega}v'_\beta\\ \dot{v}'_\beta &= \omega_{p1}(v_\beta - \hat{v}_\beta - v'_\beta) + \bar{\omega}v'_\alpha.\end{aligned} \tag{26}$$

Substituting (23) and (26) into (25) gives

$$\dot{\vartheta} \approx \frac{\omega_{p_1}\omega_{p_2}}{\hat{V}^2}\left[v_\beta\hat{v}_\alpha - v_\alpha\hat{v}_\beta\right] + \omega_{p_1}\underbrace{\frac{\omega_{p_2}}{\hat{V}^2}\left[v'_\alpha\hat{v}_\beta - v'_\beta\hat{v}_\alpha\right]}_{-\vartheta}. \tag{27}$$

Considering (20) and (21), (27) can be rewritten as

$$\begin{aligned}\dot{\vartheta} &\approx \frac{\omega_{p_1}\omega_{p_2}}{\hat{V}^2}V\hat{V}\sin(\theta-\hat{\theta}) - \omega_{p_1}\vartheta\\ &\approx \omega_{p_1}\omega_{p_2}(\theta-\hat{\theta}) - \omega_{p_1}\vartheta.\end{aligned} \tag{28}$$

Based on (22), (24), (28), and Fig. 13(a), and defining $\theta = \theta_n + \Delta\theta$, $\hat{\theta} = \theta_n + \Delta\hat{\theta}$, $\bar{\omega} = \omega_n + \Delta\bar{\omega}$, where $\theta_n = \int \omega_n dt$, the small-signal model of the 1ϕ-CBF-FLL can be obtained as depicted in Fig. 14(a). Remember that we have neglected the saturation unit during the modeling, which means $\hat{\omega} = \bar{\omega}$ and, therefore, $\Delta\hat{\omega} = \Delta\bar{\omega}$. By applying the block diagram algebra, this model can be represented as shown in Fig. 14(b).

2) Tuning: From Fig. 14(b), the open-loop transfer function (29) can be obtained as

$$G_{ol}(s) = \frac{\Delta\hat{\theta}(s)}{\Delta\theta(s)} = \frac{\omega_{p1}}{s+\omega_{p1}}\frac{\omega_{p2}s + \omega_{p2}/\tau}{s^2}. \tag{29}$$

This open-loop transfer function has two poles at the origin and a pole-zero pair, which means it is a type-2 transfer function. For such systems, using the symmetrical optimum method, which sets the gain crossover frequency at the geometric mean of the pole-zero pair to maximize the phase margin, is often recommended [7], [26]. The application of this design method to (29) gives the control parameters as follows, in which ω_c is the gain crossover frequency, and b is a phase-margin (PM) determining factor, i.e., $\mathrm{PM} = \tan^{-1}\frac{\mathrm{b}^2-1}{2\mathrm{b}}$

$$\begin{aligned}\omega_{p1} &= b\omega_c\\ \omega_{p2} &= \omega_c\\ \tau &= b/\omega_c.\end{aligned} \tag{30}$$

It is often recommended to set the design constant b equal to $b = 1+\sqrt{2}$. It corresponds to an optimum damping factor $1/\sqrt{2}$ for the closed-loop poles of the system and provides a $\mathrm{PM} = 45°$, which is good enough to ensure stability [7]. Selecting the gain crossover frequency ω_c, however, is not that straightforward as we are facing a particular situation here: Existing a large fundamental negative-sequence component in the 1ϕ-CBF-FLL input. Remember that the CBF in the 1ϕ-CBF-FLL structure sees the single-phase input as an imbalanced signal in the $\alpha\beta$ frame and tries to get rid of its negative-sequence component. Achieving this objective requires a narrow bandwidth for the CBF, and therefore, according to (30), a small value for ω_c. A very small ω_c, nevertheless, significantly slows down the 1ϕ-CBF-FLL dynamic response. Therefore, one has to make a tradeoff decision. Here, based on a trial-and-error method, $\omega_c = 2\pi 10$ rad/s is selected. Once b and ω_c are selected, all control parameters can be calculated using (30) as summarized in Table I.

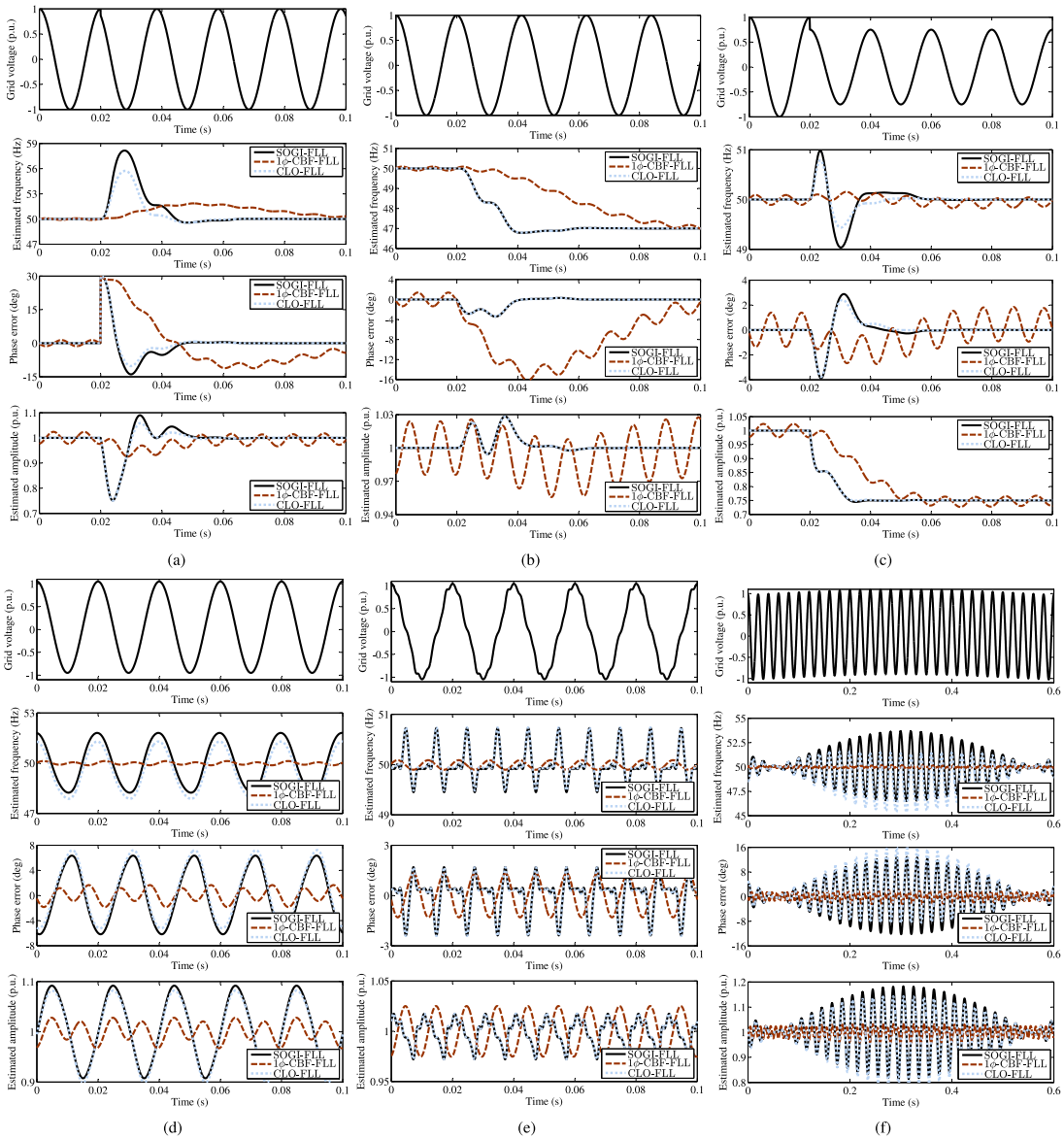

Fig. 16. Performance comparison among the SOGI-FLL, 1ϕ-CBF-FLL, and CLO-FLL. (a) Test 1. (b) Test 2. (c) Test 3. (d) Test 4. (e) Test 5. (f) Test 6.

3) Numerical Results: In this part, a numerical performance comparison between the 1ϕ-CBF-FLL and SOGI-FLL under the same tests as those explained in Section II-C1 is presented. The control parameters of both these FLLs can be found in Table I. The digital implementation of the 1ϕ-CBF-FLL is observed in Fig. 15. Notice that to achieve a high accuracy, two ROGIs in the second-order CBF structure are discretized as $G_{\mathrm{ROGI}}(z) = \frac{T_s}{z - e^{j\omega T_s}}$ [25].

In Fig. 16(a), (b), and (c), the dynamic performances of the SOGI-FLL and 1ϕ-CBF-FLL in response to a phase jump, frequency jump, and amplitude jump are compared, respectively. The first noticeable observation in these results is the presence of double-frequency oscillatory ripples in the estimated quantities by the 1ϕ-CBF-FLL. The reason behind these oscillations is that the input signal, from the CBF point of view, is imbalanced [see (19)], and the CBF cannot completely remove its fundamental negative-sequence component. This fact is more clear from Fig. 17, which illustrates the Bode magnitude plot of the second-order CBF used in the input of the 1ϕ-CBF-FLL. As highlighted in this figure, the second-order

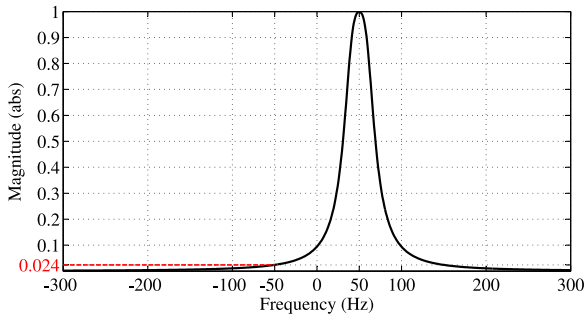

Fig. 17. Bode magnitude plot of the second-order CBF used in the input of the 1ϕ-CBF-FLL. Parameters: $\omega_{p1} = 151.7$ rad/s and $\omega_{p2} = 62.8$ rad/s.

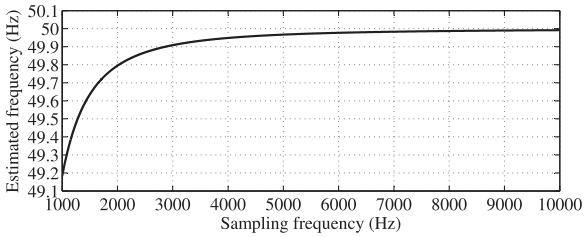

Fig. 18. Offset error of the 1ϕ-CBF-FLL frequency estimation as a function of the sampling frequency.

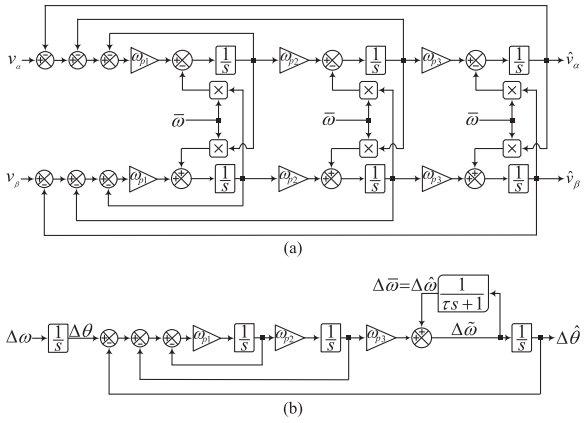

Fig. 19. (a) Third-order CBF. (b) Small-signal model of the 1ϕ-CBF-FLL when this third-order CBF is used in its structure. ω_{p1}, ω_{p2}, and ω_{p3} are the third-order CBF control parameters.

CBF has a magnitude equal to 0.024 at -50 Hz. It means that the CBF outputs have a 0.024 p.u. fundamental negative-sequence component when the input signal amplitude is 1 p.u. This negative-sequence component causes the aforementioned double-frequency oscillations. To make these oscillatory ripples smaller, we have to reduce the gain crossover frequency in the tuning procedure [see (30) and the discussion after that]. It, however, slows down the 1ϕ-CBF-FLL transient response and, therefore, may not be a great idea. Notice that the dynamic behavior of the 1ϕ-CBF-FLL is already much slower than that of the SOGI-FLL [see Fig. 16(a), (b), and (c)].

Fig. 16(d), (e), and (f) compares the SOGI-FLL and 1ϕ-CBF-FLL ability in rejecting the dc offset, low-order harmonics, and a subharmonic. Thanks to its lower bandwidth, the 1ϕ-CBF-FLL represents a much better performance in these tests, and more effectively suppress the grid voltage disturbances. The details of these numerical results can be found in Table II. A comparison between the computational burden of these FLLs may be found in Table III.

4) Further Discussions: In this part, further discussions on some problems of the 1ϕ-CBF-FLL are presented. The first issue is a frequency offset error in the 1ϕ-CBF-FLL, and the second one is the aforementioned double-frequency errors.

Assume that the $\alpha\beta$-axis outputs of the second-order CBF in Fig. 15 are in the discrete-time domain as

$$\begin{aligned}\hat{v}_\alpha(n) &= V\cos(n\omega T_s)\\ \hat{v}_\beta(n) &= V\sin(n\omega T_s)\end{aligned} \tag{31}$$

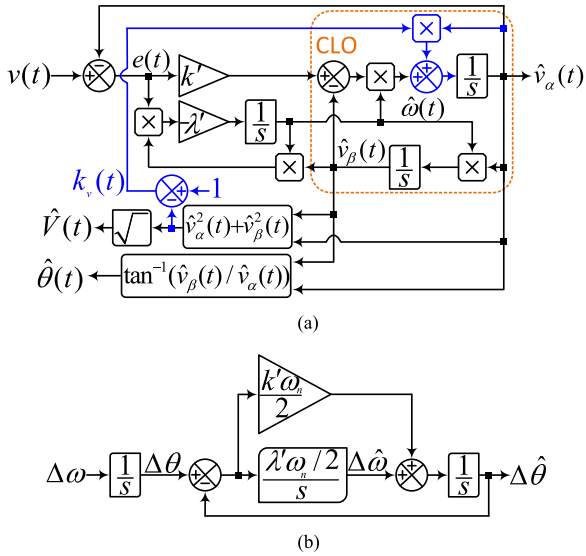

Fig. 20. (a) CLO-FLL in the continuous-time domain [12]. (b) Small-signal model of the CLO-FLL [32]. k' and λ' are the control parameters of the CLO-FLL.

where V and ω denote the grid voltage amplitude and angular frequency, and n denotes the current sample. For the sake of simplicity, it is also assumed that V and ω are constant. In this case, the estimated frequency $\tilde{\omega}$ in Fig. 15 can be expressed as

$$\begin{aligned}\tilde{\omega}(n) &= \frac{\hat{v}_\alpha(n-1)\hat{v}_\beta(n)-\hat{v}_\beta(n-1)\hat{v}_\alpha(n)}{T_s\left[\hat{v}_\alpha^2(n)+\hat{v}_\beta^2(n)\right]} = \\ &\frac{V^2\left[\cos((n-1)\omega T_s)\sin(n\omega T_s)-\sin((n-1)\omega T_s)\cos(n\omega T_s)\right]}{T_sV^2\left[\cos^2(n\omega T_s)+\sin^2(n\omega T_s)\right]} \\ &= \frac{\sin(\omega T_s)}{T_s} = \omega - \underbrace{\frac{\omega^3T_s^2}{3!}+\frac{\omega^5T_s^4}{5!}-\ldots}_{\text{error terms}}.\end{aligned} \tag{32}$$

It is clear from (32) that the estimated frequency by the 1ϕ-CBF-FLL contains an offset error. This error is negligible when the sampling frequency is high. It, however, may become noticeable at low sampling frequencies. Fig. 18 clearly demonstrates this fact. Fortunately, eliminating this error is not complicated. Indeed, it can be simply corrected by including an inverse sine function into the frequency estimation loop in Fig. 15. Some alternative approaches to correct such a frequency offset error may be found in [27]–[29].

The second issue is the presence of double-frequency oscillatory errors in the 1ϕ-CBF-FLL estimated quantities. It was discussed before that mitigating these oscillatory errors by further narrowing the FLL bandwidth may not be a good idea as it makes its dynamic response very slow. An alternative solution, as suggested in [11], is increasing the CBF order. A possible problem, in this case, is obtaining a small-signal model for the 1ϕ-CBF-FLL structure, particularly when the CBF order is very high. Fortunately, a clear pattern between the 1ϕ-CBF-FLL model and its CBF structure exists. We have demonstrated this fact before for the case of a second-order

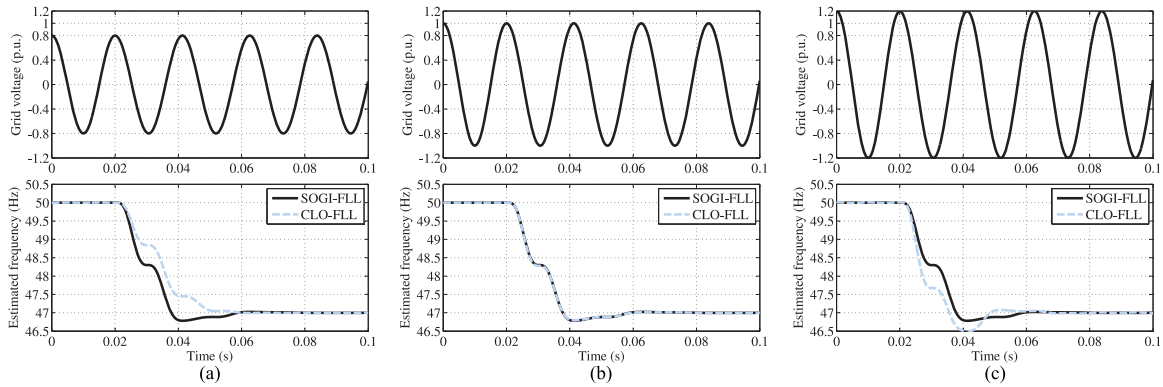

Fig. 21. Repeating Test 2 (-3-Hz frequency jump) for different values of the grid voltage amplitude. (a) $V = 0.8$ p.u. (b) $V = 1$ p.u. (c) $V = 1.2$ p.u.

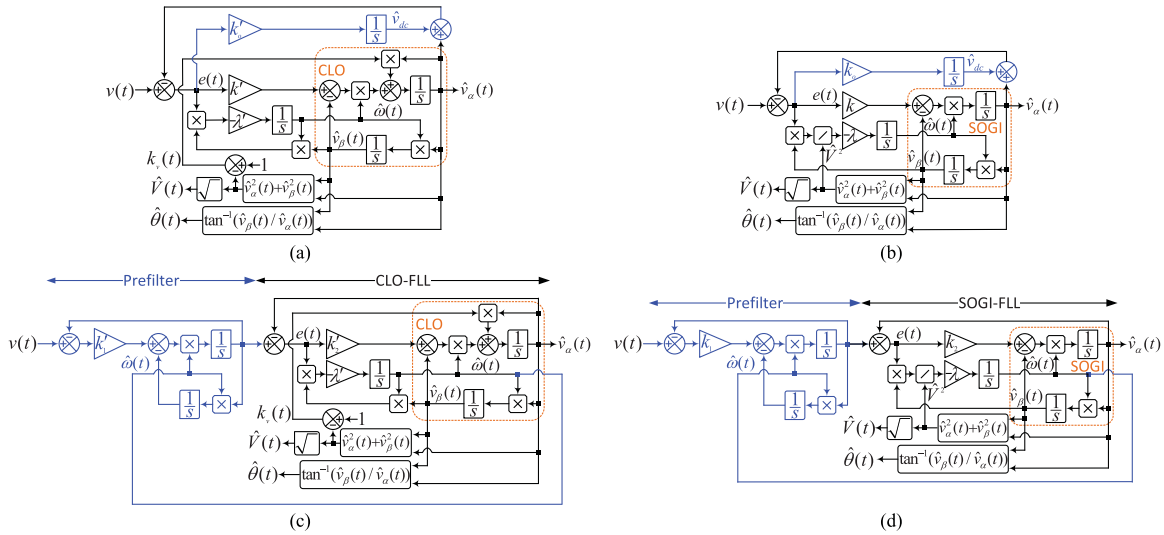

Fig. 22. (a) CLO-FLL-WDCRC [12]. (b) SOGI-FLL-WDCRC [4]. (c) CLO-FLL-WPF [32]. (d) SOGI-FLL-WPF [5].

CBF [see Figs. 13(b) and 14(a)]. To make this pattern more clear, the continuous-time implementation of a third-order CBF and the resultant model when this CBF is used in the 1ϕ-CBF-FLL structure are presented in Fig. 19. Based on this pattern, the small-signal model of the 1ϕ-CBF-FLL can be directly and easily obtained regardless of the CBF order in its structure. Once the small-signal model is derived, tuning the control parameters using the systematic approach presented in [30] is quite straightforward.

IV. CLO-FLL and Its Advanced Versions

A. Review of CLO-FLL

The basic building block of the SOGI-FLL and its advanced versions is the SOGI, which is a linear harmonic oscillator. It is briefly discussed in [12] and [31] that the SOGI has a continuum of closed orbits, which makes the SOGI-FLL and its advanced versions susceptible to disturbances such as voltage sags and swells. These works also argue that a nonlinear oscillator can offer a more robust performance compared to the SOGI under these disturbances. Based on this argument, the CLO, which is a non-linear oscillator, and the CLO-FLL are presented in [12]. The block diagram representation of the CLO-FLL in the continuous-time domain can be observed in Fig. 20(a). From the structural point of view, removing the amplitude normalization and adding a feedback loop, which is highlighted in Fig. 20(a), are the main changes in the CLO-FLL compared to the SOGI-FLL.

B. Analysis of CLO-FLL

In [32], a small-signal model for the CLO-FLL has been presented. This model, which is shown in Fig. 20(b), is the same as that of the SOGI-FLL [see Fig. 6(a)] if the following relationship between their control parameters hold[6]:

$$\begin{aligned} k' &= k \\ \lambda' &= \lambda/\omega_n. \end{aligned} \tag{33}$$

[6]In obtaining the CLO-FLL model in [32], the grid voltage amplitude is assumed to be 1 p.u. As the CLO-FLL has no amplitude normalization, this model is fairly accurate as long as the grid voltage amplitude is 1 p.u. or very close to it. Therefore, any conclusion based on this model is valid as long as the aforementioned condition holds.

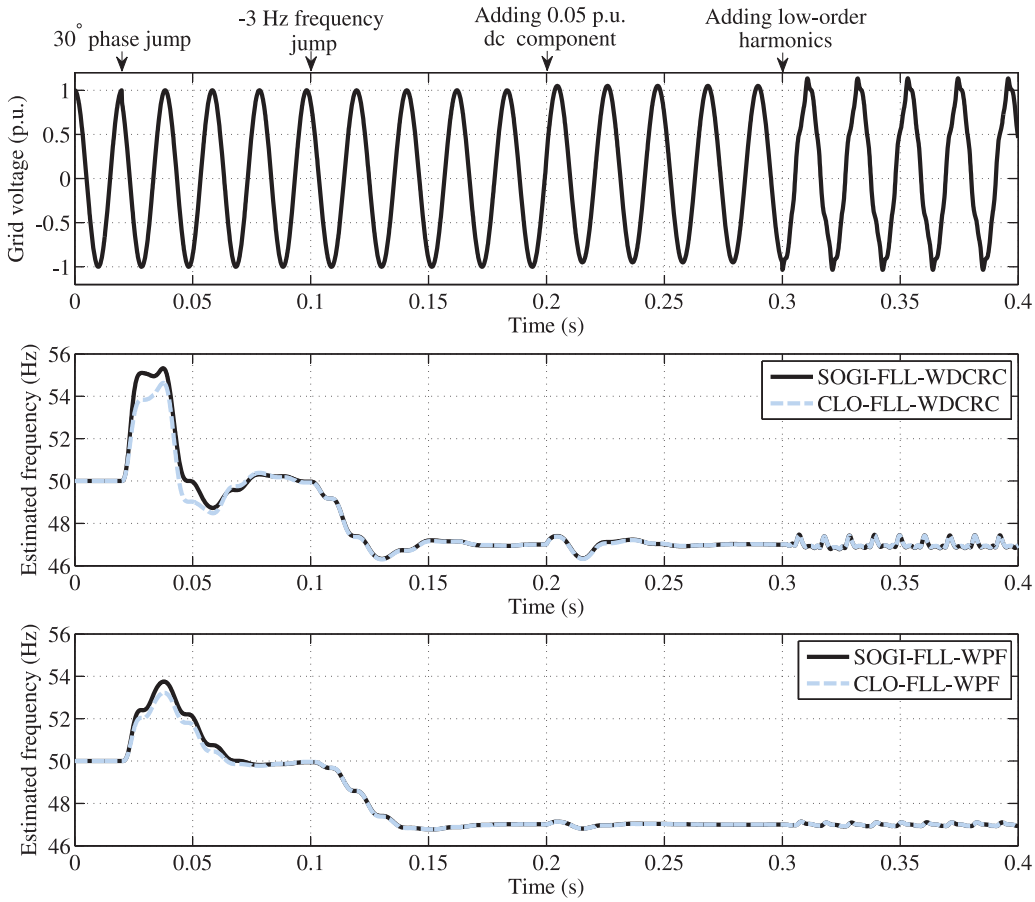

Fig. 23. Numerical performance comparison between advanced CLO-FLLs and their SOGI-based counterparts in response to different disturbances.

It implies that the CLO-FLL, contrary to the original motivation in its design, may not have a much better performance compared to the SOGI-FLL in response to different disturbances. To prove this fact, a numerical comparison between the CLO-FLL and SOGI-FLL in response to the tests described in Section II-C1 is carried out. The control parameters of the CLO-FLL are determined based on (33) [see Table I].

The obtained results are shown in Fig. 16. It is observed that the CLO-FLL demonstrates a little more damping compared to the SOGI-FLL in response to Tests 1 and 3 [see Fig. 16(a) and (c)]. In the rest of the tests, they have almost the same performance. Details of these results are summarized in Table II. The information about the CLO-FLL computational cost may be found in Table III.

In previous tests (except for Test 3), the amplitude of the grid voltage fundamental component was fixed at its nominal value. As the CLO-FLL, contrary to the SOGI-FLL, has no amplitude normalization, its performance is affected by changes in the input signal amplitude. To better visualize this fact, Test 2 is repeated for different values of the grid voltage amplitude. The obtained results, which are shown in Fig. 21, clearly demonstrate that the CLO-FLL (contrary to the SOGI-FLL) has an amplitude-dependent performance. This fact can be further supported by repeating other tests under different grid voltage amplitudes.

In summary, as long as the grid voltage amplitude is at or very close to its nominal value, there is not a large difference in the performance of the CLO-FLL and SOGI-FLL. It, however, may not be the case under voltage sags and swells. The reason is the lack of an amplitude normalization in the CLO-FLL structure, which makes its performance amplitude-dependent. This is a serious drawback in grid applications.

C. Further Discussions

To improve the CLO-FLL filtering capability, some modifications have been suggested in [12] and [32]. A brief analysis of these modifications is presented in this part.

The CLO-FLL, similar to the SOGI-FLL, has limited ability in rejecting the grid voltage dc component and suffers from fundamental-frequency oscillatory ripples in the presence of such a component. This fact is clear from Fig. 16(d). To address this problem, adding a dc rejection loop to the CLO-FLL is proposed in [12]. The block diagram representation of the resultant structure, which is here referred to as the CLO-FLL with dc rejection capability (CLO-FLL-WDCRC) can be observed in Fig. 22(a) [12]. Notice that, as mentioned before, this dc rejection loop has been originally presented in [4]. The application of this loop to the SOGI-FLL may also be observed in Fig. 22(b).

TABLE IV
CONTROL PARAMETERS OF SOGI-FLL-WDCRC, CLO-FLL-WDCRC, SOGI-FLL-WPF, AND CLO-FLL-WPF

	Parameters
SOGI-FLL-WDCRC [4]	$k = 1,\ k_o = 0.25\omega_n = 78.5,\ \lambda = 30\,000$
CLO-FLL-WDCRC	$k' = k = 1,\ k'_o = k_o = 78.5,\ \lambda' = \lambda/\omega_n = 95.5$
SOGI-FLL-WPF [7]	$k_1 = \sqrt{2},\ k_2 = \sqrt{2},\ \lambda = 23\,948$
CLO-FLL-WPF	$k'_1 = k_1 = \sqrt{2},\ k'_2 = k_2 = \sqrt{2},\ \lambda' = \lambda/\omega_n = 76.2$

The CLO-FLL also has limited harmonic filtering capability and suffers from oscillatory ripples under distorted grid conditions [see Fig. 16(e)]. To deal with the grid voltage harmonics and its dc component at the same time, using an adaptive BPF as the CLO-FLL prefilter is proposed in [32]. The block diagram representation of the CLO-FLL with prefilter (CLO-FLL-WPF) is shown in Fig. 22(c). It has to be emphasized here that this prefilter has been first presented in [5] to enhance the SOGI-FLL filtering capability [see Fig. 22(d)].

It was demonstrated in Section IV-B that there is not a large difference in the performance of the CLO-FLL and SOGI-FLL as long as the grid voltage amplitude is at or very close to its nominal value. Hence, the aforementioned advanced CLO-FLLs (i.e., the CLO-FLL-WDCRC and CLO-FLL-WPF) should have a similar relationship with their SOGI-based counterparts. This conclusion is numerically examined in what follows. The selected control parameters for this examination can be found in Table IV. Fig. 23 illustrates the results of this comparison. To save space, only estimated frequencies by the FLLs under study are shown. As predicted before, there is not a large difference in the results of the CLO-FLL-WDCRC and CLO-FLL-WPF compared to their SOGI-based counterparts.

V. SUMMARY AND CONCLUSION

Conducting a thorough analysis of the LKF-FLL, 1ϕ-CBF-FLL, and CLO-FLL, and highlighting their advantages/disadvantages compared to the SOGI-FLL were the main aims of this paper. Our focus was first on the LKF-FLL. To facilitate the study, the continuous-time equivalent of the LKF-FLL was first obtained, and its steady-state version was presented. A thorough analysis of the SSLKF-FLL was then conducted. It was demonstrated that the SSLKF-FLL is mathematically equivalent with the SOGI-FLL if its β-axis Kalman gain k'_β is set to zero. It was then shown that the SSLKF-FLL provides a rather higher dc offset/sub-harmonic rejection capability, a slightly lower harmonic filtering ability, and a little slower and more damped dynamic behavior compared to the SOGI-FLL if an optimal relationship between its Kalman gains is established. As the performance difference between this SSLKF-FLL and the SOGI-FLL is not very large, it can be concluded that they are synchronization systems of roughly comparable qualities. The study was then focused on the LKF-FLL. It was discussed theoretically that the LKF-FLL and its steady-state version have almost the same performance in the grid-connected applications because the grid voltage frequency and, therefore, the Kalman gains of the LKF-FLL have limited variations. This prediction was then confirmed using numerical and experimental tests. Considering this fact and its high computational burden, it can be concluded that the LKF-FLL may not be an attractive option for the synchronization purposes in the grid-connected applications, at least not compared to its steady-state version (SSLKF-FLL) and the SOGI-FLL. It has to be emphasized here that the same conclusion may not be necessarily valid in applications such as more electric aircraft, where very large frequency changes may happen. This issue will be investigated in future works.

In the second part of this study, the focus was on the 1ϕ-CBF-FLL. For the sake of simplicity in the analysis, a second-order CBF was considered. The 1ϕ-CBF-FLL modeling and tuning were then discussed, and a numerical comparison with the SOGI-FLL was conducted. It was observed that the 1ϕ-CBF-FLL offers a higher dc/subharmonic/harmonic filtering capability than the SOGI-FLL. It, however, suffers from double-frequency oscillatory ripples and a slower dynamic response. These qualities are due to the 1ϕ-CBF-FLL structure and its narrow bandwidth, which is required to make the aforementioned ripples small. It was also demonstrated that 1ϕ-CBF-FLL suffers from a frequency offset error at low sampling frequencies, and a simple solution to correct it was proposed. An intuitive approach to easily derive the 1ϕ-CBF-FLL small-signal model when higher order CBFs are used in its structure was also presented.

In the last part of this study, an investigation on the CLO-FLL was conducted. It was discussed theoretically and verified numerically that there is not a large difference in the performance of the CLO-FLL and SOGI-FLL as long as the grid voltage amplitude is at (or very close to) its nominal value. It was also demonstrated that the CLO-FLL (contrary to the SOGI-FLL) has an amplitude-dependent performance, which is a serious drawback in grid applications. A study on two advanced versions of the CLO-FLL, called the CLO-FLL-WDCRC and CLO-FLL-WPF, was also conducted. It was observed that there is not a large difference in the performance of the CLO-FLL-WDCRC and CLO-FLL-WPF compared to their SOGI-based counterparts, i.e., SOGI-FLL-WDCRC and SOGI-FLL-WPF.

The discussions and results of this paper provide a good insight into the LKF-FLL, 1ϕ-CBF-FLL, and CLO-FLL characteristics and their advantages/disadvantages compared to the SOGI-FLL, which is a standard structure. This knowledge can be beneficial for researchers who are working in this area and want to make further contributions.

ACKNOWLEDGMENT

The authors would like to acknowledge with thanks the Deanship of Scientific Research (DSR) for technical and financial support.

REFERENCES

[1] B. K. Bose, "Global energy scenario and impact of power electronics in 21st century," *IEEE Trans. Ind. Electron.*, vol. 60, no. 7, pp. 2638–2651, Jul. 2013.

[2] H. A. Hamed, A. F. Abdou, E. H. E. Bayoumi, and E. E. EL-Kholy, "A fast recovery technique for grid-connected converters after short dips using a hybrid structure PLL," *IEEE Trans. Ind. Electron.*, vol. 65, no. 4, pp. 3056–3068, Apr. 2018.

[3] P. Rodriguez, A. Luna, I. Candela, R. Mujal, R. Teodorescu, and F. Blaabjerg, "Multiresonant frequency-locked loop for grid synchronization of power converters under distorted grid conditions," *IEEE Trans. Ind. Electron.*, vol. 58, no. 1, pp. 127–138, Jan. 2011.

[4] M. Karimi-Ghartemani, S. A. Khajehoddin, P. K. Jain, A. Bakhshai, and M. Mojiri, "Addressing DC component in PLL and notch filter algorithms," *IEEE Trans. Power Electron.*, vol. 27, no. 1, pp. 78–86, Jan. 2012.

[5] J. Matas, M. Castilla, J. Miret, L. G. de Vicuna, and R. Guzman, "An adaptive prefiltering method to improve the speed/accuracy tradeoff of voltage sequence detection methods under adverse grid conditions," *IEEE Trans. Ind. Electron.*, vol. 61, no. 5, pp. 2139–2151, May 2014.

[6] Z. Xin, R. Zhao, P. Mattavelli, P. C. Loh, and F. Blaabjerg, "Reinvestigation of generalized integrator based filters from a first-order-system perspective," *IEEE Access*, vol. 4, pp. 7131–7144, 2016.

[7] S. Golestan, J. M. Guerrero, J. C. Vasquez, A. M. Abusorrah, and Y. A. Al-Turki, "Modeling, tuning, and performance comparison of second-order generalized integrator-based FLLs," *IEEE Trans. Power Electron.*, vol. 33, no. 12, pp. 10 229–10 239, Dec. 2018.

[8] M. S. Reza, M. Ciobotaru, and V. G. Agelidis, "Accurate estimation of single-phase grid voltage fundamental amplitude and frequency by using a frequency adaptive linear Kalman filter," *IEEE J. Emerg. Sel. Topics Power Electron.*, vol. 4, no. 4, pp. 1226–1235, Dec. 2016.

[9] M. S. Reza, M. Ciobotaru, and V. G. Agelidis, "Instantaneous power quality analysis using frequency adaptive Kalman filter technique," in *Proc. 7th Int. Power Electron. Motion Control Conf.*, Jun. 2012, vol. 1, pp. 81–87.

[10] M. S. Reza, M. Ciobotaru, and V. G. Agelidis, "Frequency adaptive linear Kalman filter for fast and accurate estimation of grid voltage parameters," in *Proc. IEEE Int. Conf. Power Syst. Technol.*, Oct. 2012, pp. 1–6.

[11] C. A. Busada, H. G. Chiacchiarini, and J. C. Balda, "Synthesis of sinusoidal waveform references synchronized with periodic signals," *IEEE Trans. Power Electron.*, vol. 23, no. 2, pp. 581–590, Mar. 2008.

[12] H. Ahmed, S. Amamra, and M. H. Bierhoff, "Frequency-locked loop based estimation of single-phase grid voltage parameters," *IEEE Trans. Ind. Electron.*, to be published.

[13] R. E. Kalman, "A new approach to linear filtering and prediction problems," *J. Basic Eng.*, vol. 82, no. 1, pp. 35–45, 1960.

[14] R. E. Kalman and R. S. Bucy, "New results in linear filtering and prediction theory," *J. Basic Eng.*, vol. 83, no. 1, pp. 95–108, 1961.

[15] J. Meng, G. Luo, and F. Gao, "Lithium polymer battery state-of-charge estimation based on adaptive unscented Kalman filter and support vector machine," *IEEE Trans. Power Electron.*, vol. 31, no. 3, pp. 2226–2238, Mar. 2016.

[16] A. Rouhani and A. Abur, "Constrained iterated unscented Kalman filter for dynamic state and parameter estimation," *IEEE Trans. Power Syst.*, vol. 33, no. 3, pp. 2404–2414, May 2018.

[17] S. Golestan, J. M. Guerrero, and J. C. Vasquez, "Steady-state linear Kalman filter-based PLLs for power applications: A second look," *IEEE Trans. Ind. Electron.*, vol. 65, no. 12, pp. 9795–9800, Dec. 2018.

[18] K. D. Brabandere *et al.*, "Design and operation of a phase-locked loop with Kalman estimator-based filter for single-phase applications," in *Proc. 32nd Annu. Conf. IEEE Ind. Electron.*, Nov. 2006, pp. 525–530.

[19] L. Xie, D. Popa, and F. L. Lewis, *Optimal and Robust Estimation: With an Introduction to Stochastic Control Theory*. Boca Raton, FL, USA: CRC Press, 2007.

[20] S. Golestan, E. Ebrahimzadeh, J. M. Guerrero, and J. C. Vasquez, "An adaptive resonant regulator for single-phase grid-tied VSCs," *IEEE Trans. Power Electron.*, vol. 33, no. 3, pp. 1867–1873, Mar. 2018.

[21] *Voltage Characteristics of Electricity Supplied by Public Distribution Systems*, BSI Standard EN 50160, 1999.

[22] W. Li, X. Ruan, C. Bao, D. Pan, and X. Wang, "Grid synchronization systems of three-phase grid-connected power converters: A complex-vector-filter perspective," *IEEE Trans. Ind. Electron.*, vol. 61, no. 4, pp. 1855–1870, Apr. 2014.

[23] E. Guest and N. Mijatovic, "Discrete-time complex bandpass filters for three-phase converter systems," *IEEE Trans. Ind. Electron.*, vol. 66, no. 6, pp. 4650–4660, Jun. 2019.

[24] X. Quan, X. Dou, Z. Wu, M. Hu, and A. Q. Huang, "Complex-coefficient complex-variable filter for grid synchronization based on linear quadratic regulation," *IEEE Trans. Ind. Informat.*, vol. 14, no. 5, pp. 1824–1834, May 2018.

[25] C. A. Busada, S. G. Jorge, A. E. Leon, and J. A. Solsona, "Current controller based on reduced order generalized integrators for distributed generation systems," *IEEE Trans. Ind. Electron.*, vol. 59, no. 7, pp. 2898–2909, Jul. 2012.

[26] S. Preitl and R.-E. Precup, "An extension of tuning relations after symmetrical optimum method for PI and PID controllers," *Automatica*, vol. 35, no. 10, pp. 1731–1736, 1999.

[27] S. Golestan, A. Vidal, A. G. Yepes, J. M. Guerrero, J. C. Vasquez, and J. Doval-Gandoy, "A true open-loop synchronization technique," *IEEE Trans. Ind. Informat.*, vol. 12, no. 3, pp. 1093–1103, Jun. 2016.

[28] P. Kanjiya, V. Khadkikar, and M. S. E. Moursi, "A novel type-1 frequency-locked loop for fast detection of frequency and phase with improved stability margins," *IEEE Trans. Power Electron.*, vol. 31, no. 3, pp. 2550–2561, Mar. 2016.

[29] P. Kanjiya, V. Khadkikar, and M. S. E. Moursi, "Obtaining performance of type-3 phase-locked loop without compromising the benefits of type-2 control system," *IEEE Trans. Power Electron.*, vol. 33, no. 2, pp. 1788–1796, Feb. 2018.

[30] S. Golestan, F. D. Freijedo, and J. M. Guerrero, "A systematic approach to design high-order phase-locked loops," *IEEE Trans. Power Electron.*, vol. 30, no. 6, pp. 2885–2890, Jun. 2015.

[31] E. Oviedo, N. Vazquez, and R. Femat, "Synchronization technique of grid-connected power converters based on a limit cycle oscillator," *IEEE Trans. Ind. Electron.*, vol. 65, no. 1, pp. 709–717, Jan. 2018.

[32] M. L. Pay and H. Ahmed, "Modeling and tuning of circular limit cycle oscillator FLL with pre-loop filter," *IEEE Trans. Ind. Electron.*, to be published.

Authors' photographs and biographies not available at the time of publication.